

# Optimal photometry for colour-magnitude diagrams and its application to NGC 2547

Tim Naylor<sup>1,2</sup>, E.J. Totten<sup>2</sup>, R.D. Jeffries<sup>2</sup>, M. Pozzo<sup>2,3</sup>, C.R. Devey<sup>2</sup> and S.A. Thompson<sup>2</sup>

<sup>1</sup>*School of Physics, University of Exeter, Stocker Road, Exeter EX4 4QL*

<sup>2</sup>*Department of Physics, Keele University, Staffordshire, ST5 5BG*

<sup>3</sup>*Imperial College of Science, Technology and Medicine, Blackett Laboratory, Prince Consort Road, London SW7 2BW*

## ABSTRACT

We have developed the techniques required to use the optimal photometry algorithm of Naylor (1998) to create colour-magnitude diagrams with well defined completeness functions. To achieve this we first demonstrate that the optimal extraction is insensitive to uncertainties in the star’s measured position. We then show how to correct the optimally extracted fluxes such that they correspond to those measured in a large aperture, so aperture photometry of standard stars can be used to place the measurements on a standard system. The technique simultaneously removes the effects of a position dependent point-spread function. Finally we develop a method called “ghosting”, which calculates the completeness corrections in the absence of an accurate description of the point spread function.

We apply these techniques to the young cluster NGC 2547 (=C0809-491), and use an X-ray selected sample to find an age of 20-35Myr and an intrinsic distance modulus of 8.00-8.15 magnitudes. We use these isochrones to select members from our photometric surveys. Our derived luminosity function shows a well defined Wielen dip, making NGC 2547 the youngest cluster in which such a feature has been observed. Our derived mass function spans the range 0.1-6 $M_{\odot}$  and is similar to that for the field and the older, more massive clusters M35 and the Pleiades, supporting the idea of a universal initial mass function.

**Key words:** techniques: image processing – techniques: photometric – methods: data analysis – open clusters and associations: individual: NGC 2547 – stars: formation – stars: pre-main-sequence

## 1 INTRODUCTION

Naylor (1998) presented a new method of carrying out photometry for digital images, weighting each pixel according to its signal-to-noise ratio. Aside from the obvious improvement in signal-to-noise ratio, this “optimal photometry” offers over traditional aperture methods, it also provides robust error bar estimation, freedom from bias incurred by mis-estimating the point spread function (PSF), and ease of automation. The possibility of such a scheme was first suggested by Stover & Allen (1987) (we were unaware of this work when we published Naylor 1998), although they did not apply fully optimal masks, or realize the full importance of using the same weighting for all stars. We originally developed optimal photometry for differential time-series work, and in Naylor (1998) explicitly ignored the problems that would be posed were it applied to colour-magnitude diagrams (CMDs). Since other groups are now beginning to utilize optimal photometry, and it is becoming more widely

available (see, for example, the Starlink release Eaton et al. 1999), it would seem timely to rectify this omission. Motivated by a scientific desire to obtain the most precise photometry possible from data on young stellar clusters and associations, along with a reliable estimate of the fraction of stars detected at a given flux level, we have now developed the techniques required. In this paper we use them to derive a mass function for the young open cluster NGC2547 (= C0809-491). However, it is important to emphasize that the algorithms have been developed whilst we have been working on datasets from a range of telescopes, instruments and targets (including  $J, H, K$  IR data). The first result to be published was our study of low-mass stars around  $\gamma^2$  Velorum (Pozzo et al. 2000), and more publications are in preparation (Totten et al. 2000; Naylor et al. 2001).

This work should be seen in the context of a host of other observational projects currently underway, and data reduction programmes now available. The most illuminating

comparisons are with projects which, like ours, concentrate on colour-magnitude diagrams. These include the CFHT Cluster Survey (Kalirai et al. 2001), the WIYN Open Cluster Survey (von Hippel & Sarajedini 1998) and the ESO pre-FLAMES survey (Momany et al. 2001; Arnouts et al. 2001). Not only do we share data reduction aims with these surveys, but our observational techniques are forced to be broadly similar (though there are important differences in detail). In contrast the very large surveys often have specialized data acquisition techniques, whether they survey a large area of sky, such as the Sloan Digital Sky Survey (York et al. 2000), DENIS (Epchtein et al. 1997) and 2MASS; or whether they aim to detect variability such as OGLE (Udalski et al. 1997) and MACHO (Alcock et al. 1996). Algorithmically, there are two main differences between all these surveys and our work. The first is that we make final photometric measurements using optimal extraction. In contrast most of the other projects use some type of profile fitting. This is often either background determination followed by empirical profile fitting based on DAOPHOT (Stetson 1987), or simultaneous background and analytical profile fitting, based on SExtractor (Bertin & Arnouts 1996). The second major algorithmic difference is that rather than adding images of the same field together, and then carrying out the photometry, we have chosen to extract photometric measurements from each image, and then combine the measurements. Our reasons for preferring this method are outlined in Section 3.

### 1.1 NGC 2547

The open cluster NGC2547 (= C0809-491) lies at Galactic co-ordinates  $l = 264.45^\circ$   $b = -8.53^\circ$  ( $\alpha = 08\ 10\ 25.7$ ,  $\delta = -49\ 10\ 03$ ; J2000). Clariá (1982) placed it at a distance of 450pc with a reddening of  $E(B - V) = 0.06$  and an age of 57Myr. This age is close to that of  $\alpha$  Per ( $\simeq 50$ Myr) and Jeffries & Tolley (1998) sought to use it as a comparison to ascertain if age was the main driver of cluster properties such as coronal activity among low-mass stars. In doing so they discovered that fitting isochrones to the  $V$  vs.  $V - I_c$  colour-magnitude diagram for the low-mass stars, implied an age of only  $14 \pm 4$ Myr. Furthermore, they discovered very little scatter of the stars about the isochrones, beyond that attributable to binary systems and photometric errors. It is this latter property which attracts us to NGC 2547 as a testbed for our new photometry techniques. Reproducing the narrow pre-main-sequence, where the stars are widely dispersed over several CCD fields is a stringent test of both aperture correction and correctly allowing for the spatial dependence of the point spread function. Furthermore, as we have already reduced the same dataset using aperture photometry, a direct comparison is possible. Finally, the data were clearly suitable to yield a further scientific result, namely the cluster mass function. NGC 2547 is sufficiently young that it is unlikely to have suffered equipartition and dynamical evaporation of its low-mass members, so the present day mass function may be representative of the *initial* mass function. In addition, it seems likely that NGC 2547 is much less massive than previously well studied open clusters like the Pleiades and NGC 2516 (it has far fewer early-type stars). We therefore have the opportunity to see whether the mass function varies with total cluster mass or is scale invariant.

### 1.2 An outline of the paper

To help the reader keep sight of how the various parts of the reduction process are linked, we will outline the reduction process, and hence the structure of the paper. We begin by outlining the observations in Section 2. There are multiple images in each band for all of our fields. Optimal photometry forces us to measure each star separately on each image, and then combine the results (Section 3). To do so we must consider the effects of mis-centering the mask on the accuracy of our results, and we derive this for optimal photometry in Sections 3.1 and 3.2. We have found there are significant advantages to be gained by tying our source detection algorithm to our photometry technique, so the former is outlined in Section 4.

At the same time as detecting the stars, we find their positions. This involves the only significant difference between the extraction code presented in Naylor (1998) and that used here. For largely historical reasons the old version of the code determined the position of the star by fitting a Gaussian to a region 50 pixels square centered on the approximate position of the star. We now use a box whose side is twice the full width at half maximum (FWHM) of the star. In addition to a large increase in speed, this change has the considerable advantage that it is much less likely there will be a second star in the region (such a star then has to be fitted). Indeed, if there is significant flux from a second star within this box, then the optimal photometry itself will be compromised, and the star will also have been flagged as “non-stellar” (see Section 4). We are therefore unconcerned if the position is slightly inaccurate, and so we can now always limit ourselves to fitting a single Gaussian. After the positions have been determined, optimal photometry is then carried out as described in Naylor (1998).

We then discuss the most serious problem we encountered in creating colour-magnitude diagrams. We anticipated that we would have to carry out the equivalent of aperture correction, which we call profile correction (Section 6). What we did not foresee is that the correction would be a strong function of position, but as we show in Section 6.2, dealing with this turns out to be a tractable problem.

After combining measurements of the same star from different images (Section 7) we obtain astrometric positions for the stars (Section 8). We next apply our photometric solution and compare our results for NGC2547 with those in the literature (Sections 9 and 10). We then fit isochrones to the X-ray selected members to determine the cluster’s age and distance (Section 11). The fitted isochrones allow us to select cluster members (Section 12), but of course we cannot use this to derive a mass function until we know how complete the catalogue is. Thus Section 13 presents our method of deriving the completeness correction. The reason we cannot use standard techniques for this is that they require an accurate knowledge of the point spread function, thus we have developed a technique we call “ghosting”. We can then derive the cluster luminosity and mass functions (Sections 14 and 15 respectively). The resulting mass function is similar to other clusters, giving us confidence in our techniques. Finally, in Section 16 we present our conclusions and recommendations.

## 2 OBSERVATIONS

The observations were obtained in 1996 March using a 2048<sup>2</sup> CCD mounted at the Cassegrain focus of the CTIO 0.9-m telescope. This yielded a field of view of approximately  $13 \times 13$  arcminutes. Full details are given in Jeffries & Tolley (1998), but the important point for this work is that the data consisted of two  $BVI_c$  surveys, both centered on the cluster. A deep survey of 4 CCD fields covered the central regions of the cluster, whilst a wide survey of 9 fields covered the same central regions, and a contiguous outer area. With one exception, the wide survey consisted of both a long and a short exposure for each field in each band, whilst the deep survey was of 3 equal length exposures in each field in each band. The exposure times are given in Table 1.

Common practice is to move the telescope between each exposure in a series, such as our deep fields. This has the effect of moving the bad columns around the sky, so that all stars within the survey “box” will be measured in some frames. In addition it breaks up any residual flatfield or night sky emission line fringing effects. However, it also gives a non-uniform limiting magnitude to the final catalogue. For our observations the telescope was not moved, yielding a more uniform limiting magnitude, but meaning that we have not covered the entire area of sky within our survey box. Which strategy is best depends on the primary purpose of the observations. For deriving a mass function the shape of the area surveyed is unimportant, but simplicity of the completeness correction is valuable. In addition our limiting magnitude lies well above any flatfield effects, and so our strategy of not moving the telescope is well suited to the experiment in hand.

Standard stars were observed on all nights, but as stated in Jeffries & Tolley (1998), these observations showed that only the long exposures for the wide survey were taken in photometric conditions. For consistency we reduced the standard stars for this night using the aperture techniques outlined here and in Naylor (1998). The resulting zero points were fitted assuming linear colour terms. For the V-band we found we had to add (in quadrature) an additional, magnitude independent uncertainty of 0.017 magnitudes to obtain a  $\chi^2_\nu$  of about one, but that essentially no such increase was required in  $B - V$  or  $V - I_c$ .

It should be noted that the reddest standards observed had a  $V - I_c$  of 2.7 and  $B - V$  of 2.2.

## 3 COMBINING THE IMAGES

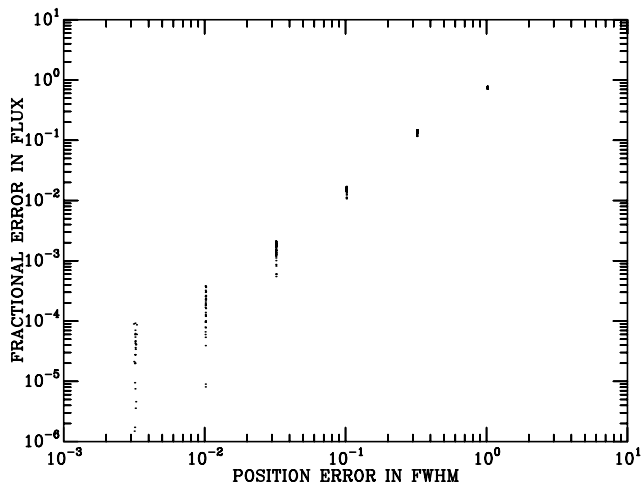
Given that one has several images of the same field, there are broadly two ways to proceed. The first is to simply add all the images together, and perform photometry on the combined image. The second is to carry out photometry on each image individually, and then combine the results for each star. The problem with adding several images together is that images of poor seeing, or high sky background will compromise the signal-to-noise ratio available from the better quality images. Despite this, other projects aiming to create colour-magnitude diagrams (see Section 1) have taken this approach. To precisely align the images they must then rebin the data into sub-pixels before adding the images using an algorithm such as “drizzle” (Mutchler & Fruchter

1997). This procedure removes the statistical independence of the pixels in the final images, complicating noise estimates. Thus we believe the correct approach is to extract photometric measurements for each star from each image, and then combine them by a weighted mean. There is another, probably more important consideration which forces us to the same conclusion. We find that our profile correction technique works well for individual images, but that the scatter about the fit described in Section 6 increases if several images are added together. We have no convincing explanation of this effect, but it gives an additional reason for dealing with individual frames. There are three final reasons for adopting this approach. First, the profile correction is probably the limiting factor at high signal-to-noise ratios, and by measuring each star in many frames we average out the effects of errors in its determination. Second, stars which lie on bad pixels in one image, may not do so in other images. Combining the measurements, not the images, allows one to obtain good photometry for these stars by simply rejecting the affected data, rather than by resorting to an image patching algorithm. Third, by testing for consistency between the different measurements of the same star we can find either variable stars, or objects which have landed on uncatalogued chip defects (see Section 7).

There are two disadvantages of using individual images, both related to faint objects. The first is that faint sources visible in a summed image are simply not detected in individual images. Secondly, if one centroids a faint source, the resulting flux will be biased in such a way as to be too bright (see Naylor 1998). Thus measuring a faint source in several images can result in a spectacular bias. The solution to these problems is to run the source detection algorithm, and position measurement on a summed frame. Since we are only interested in relatively bright stars (say signal-to-noise ratio better than 10), it does not matter that measurements of stars in this image do not reach the signal-to-noise ratios obtainable from combining measurements from individual images. The detection can be performed at a signal-to-noise ratio of, say, three, and spurious sources removed when the final catalogue is made. If a lower signal-to-noise ratio cut-off were required Fischer & Kochanski (1994) shows that once the detection cell size is chosen, it is possible to calculate the weightings required for each image to maximize the signal-to-noise ratio in the summed image. We can also take the positions measured in the summed frame, translate them into the individual frames, and fix them when performing the photometry. This avoids the centroid biasing in an analogous manner to the procedure outlined in Naylor (1998) for time series work on eclipsing binaries. The only issue we must address, is that the translation of the co-ordinates from the summed image to the individual images must be accurate enough not to affect the resulting photometry. To solve this problem, we must assess how sensitive the optimal extraction is to mis-centering of the mask. The one problem we have not been able to solve for the combined images is that of bad pixels. Practically we find we have to patch these (using a median of the surrounding data) before the individual frames are combined. This will have a small effect on the astrometry, but not of course on the photometry.

**Table 1.** Log of Observations.

Field number	Field Center (J2000)		Exposures (s)		
	R.A.	Dec.	<i>B</i>	<i>V</i>	<i>I<sub>c</sub></i>
1	08 10 37.4	-49 17 40	3×200	3×100	3×80
2	08 09 33.6	-49 17 40	3×200	3×100	3×80
3	08 10 37.5	-49 07 10	3×200	3×100	3×80
4	08 09 33.6	-49 07 10	3×200	3×100	3×80
7	08 09 07.7	-49 23 30	30, 250	15, 100	15, 100
8	08 10 12.0	-49 23 30	30, 250	15, 100	15, 100
9	08 11 16.3	-49 23 30	30, 250	15, 100	15, 100
12	08 11 16.3	-49 13 00	30, 250	15, 100	15, 100
13	08 10 12.0	-49 13 00	2×30, 250	100	2×15, 100
14	08 09 07.7	-49 13 00	30, 250	15, 100	15, 100
17	08 09 07.7	-49 02 30	30, 250	15, 100	15, 100
18	08 10 12.0	-49 02 30	30, 250	15, 100	15, 100
19	08 11 16.3	-49 02 30	30, 250	15, 100	15, 100

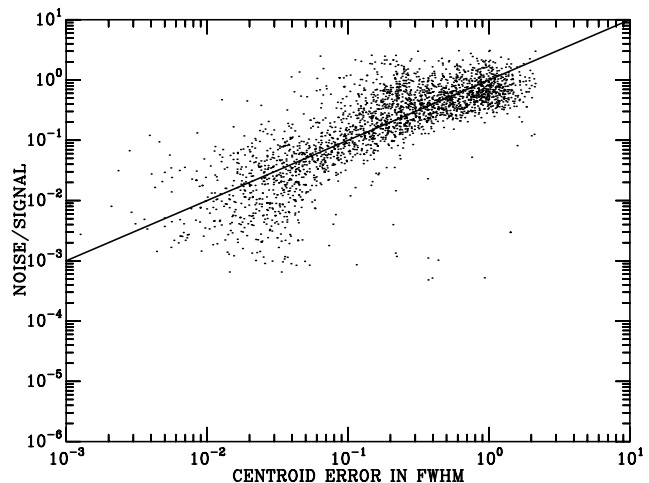
**Figure 1.** The error in the flux measurement as a function of the distance the extraction mask is mis-centered.

### 3.1 The mask mis-centering error

In Naylor (1998) we assumed that the centering of the mask was perfect, and did not contribute a significant error to the photometry. However, since the optimal mask is strongly weighted towards the center of the star, it is clear that it is more sensitive to mis-centering errors than aperture photometry. To assess this sensitivity we measured the flux from each of ten stars through a series of masks that were deliberately offset from the measured centroid. For each star and each mis-centering distance, we made four estimates of the flux at the four cardinal points with respect to the pixel grid. We then divided these off-center estimates by the on-center one to discover the fractional error the mis-centering produced. The results are shown in Fig. 1. The most important conclusion from this plot is that only when the centering error approaches a tenth of a FWHM does the error in flux exceed one percent.

### 3.2 The centroid error

To determine if the mask centering is contributing a significant error, we now need to estimate how accurately we are

**Figure 2.** The error in the measurement of the position of a star as a function of the signal-to-noise ratio. The solid line corresponds to an error of the FWHM divided by the signal-to-noise ratio.

centering the mask as a function of signal-to-noise ratio. To assess this, we measured a set of star positions on a long and a short exposure of the same field. We then calculated a six-coefficient transformation of the long-frame positions to the short-frame ones, and examined the residuals (Fig. 2). The majority of the plot follows the rule that the error in the centroid is approximately the FWHM of the image divided by the photometric signal-to-noise ratio (King 1983). Only when the centroid error declines to about 0.04FWHM, do we see significant deviation from this rule, when the error becomes independent of the signal-to-noise ratio. This corresponds to about a tenth of a pixel, and presumably subtle effects in the CCD, such as charge transfer “coma” and intra-pixel sensitivity conspire to make this the smallest uncertainty one can obtain without more sophisticated analysis (e.g. Zacharias et al. 2000).

To combine the results of this section with that above, we next require that the uncertainty in the photometry as a result of mis-centering is significantly less than the photon induced noise, for a given centroid error. Fig. 2 can be

viewed as giving the fractional photon noise as a function of centroid error. Similarly, Fig. 1 gives the fractional error in flux as a result of mis-centroiding. Since the points in Fig. 1 lie comfortably below those in Fig. 2 until the signal-to-noise ratio falls to about one, the centroiding error is always a negligible contributor to the signal-to-noise ratio for all practical cases. Further, our six-coefficient solution will always provide accurate enough positions that we can fix the positions in each frame.

#### 4 OBJECT DETECTION

The star detection algorithm is closely tied to the photometry technique. We measure the sky in boxes sufficiently large that, when the sky determination is subtracted from a star, the noise from the sky measurement is negligible (see Naylor 1998), and then subtract an interpolated sky from each pixel. Since the sky is determined by fitting a skewed Gaussian, at the same time we find the standard deviation of the sky, excluding star pixels. We then smooth the image using a simple top-hat filter, whose width is the nearest value of  $2N+1$  to four-thirds of the seeing in pixels. As shown in Naylor (1998), an aperture whose diameter is four-thirds of the FWHM seeing yields the best signal-to-noise ratio for simple aperture photometry of sky-limited objects. Thus smoothing the image in this way is equivalent to a sliding cell detection algorithm whose cell size is optimized for faint objects. We can then find which pixels are  $n\sigma$  above the noise, and use a simple north-south-east-west connectivity condition to create a list of stars (see, for example Irwin 1997).

The main problem with such a simple technique is that stars in the wings of other stars are lost where the flux does not fall to  $n\sigma$  above sky between their images, as the connectivity condition assumes they are part of the same image. We therefore begin by thresholding the image at many tens of  $\sigma$ , to create an initial list of stars. We then re-threshold the image at a  $\sigma$  level a factor of a few lower. If a star from the previous list lies within one of the new objects, the new object is discarded, otherwise it is added to the list of stars. We repeat this process, lowering the sigma level a factor of a few at a time, until the required level is reached.

The final task of the star finder is to assess which objects will have their photometry significantly affected by the presence of a nearby companion star. Although we refer to such objects as non-stellar, we wish to be clear that the aim is not to find close visual binaries, merely to reject objects whose position on the CMD is significantly affected by another star or stars. We can crystallize this definition by recalling that the integral under a two dimensional Gaussian reaches 99 percent of its full value at a radius of 1.3 FWHM. Thus the optimal photometry of a pair of equally bright stars will be affected at less than the 1 percent level by the presence of a companion 2.6 FWHM distant. Thus, we would wish that each component is marked as “stellar”. Given that we wish to measure the flux through a mask of radius twice the FWHM, the question is whether there are any deviations of the stellar profile within that radius that, when folded through the mask, total more than some given threshold. Thus our criterion is that we compare the flux extracted through a mask whose FWHM corresponds to that of the star (so roughly a normal extraction), with that ex-

tracted using a mask whose FWHM is half that of the star. Thus the second extraction is representative of the central regions of the star. We demand that this ratio is within three  $\sigma$  of the median, where the  $\sigma$  used is the sum in quadrature of the uncertainty for each measurement and the (clipped) RMS about the median. Of course we have no information as to whether saturated objects are stellar or not, so we examine these objects in a short exposure, should one have been taken. Thus the final output from this programme is a list of stars on which photometry is to be performed, with non-stellar objects flagged, and a list of stellar objects, which can be used as PSF stars.

At this point it is useful to compare our choice of algorithms with those in SExtractor (Bertin & Arnouts 1996). The comparison is particularly interesting, since SExtractor is designed to work well with low surface brightness galaxies, in contrast to our emphasis on unblended point sources. Bertin & Arnouts (1996) considered sky estimation schemes similar to ours, and although acknowledging them as the best, rejected them on the grounds of computational cost. Instead, they estimate the background as 2.5 times the median minus 1.5 times the mean. In our case, we have not found the extra compute time has a significant impact on the overall processing time, perhaps because we only search for sources once per field, but then carry out photometry on many images. Both software packages use a thresholding technique to detect the stars. SExtractor needs the flexibility to convolve the data with a range of possible shapes, whilst we only have to deal with point sources, hence our choice of the simple top hat filter. We tried varying the size of the filter, but as one might expect (see, for example, the discussion of aperture size in Naylor 1998) this has only a very small effect on the detectability of sources. Finally, SExtractor takes great care over deblending. We simply wish establish whether the object is sufficiently uncontaminated for optimal photometry, and although using a similar “tree” method, can apply simpler criteria.

#### 5 OPTIMAL PHOTOMETRY

Before carrying out optimal photometry, we must decide what mask to use. In contrast to our time series work (where a PSF star could be chosen by hand), our plethora of fields requires an automated procedure to choose a good PSF star. Our solution is to fit elliptical Gaussians to the brightest 49 unsaturated “stellar” objects, pick the star whose geometric mean FWHM is the median of the list, and fix the mask parameters at the fitted values for that star. We then perform optimal photometry of all the objects detected in the field.

From the point at which photometry of an object is attempted, the measurement carries with it an integer flag between zero and nine, where zero indicates no known problem. Each possible problem is allocated a unique number, which is written into the flag if it occurs; thus later problems overwrite any flag written by earlier ones. This process begins by writing to the flag if the detection algorithm has determined that the star is non-stellar. During the optimal photometry procedure, the object’s flag is changed if it is too close to the detector edge for any stage of the photometry process; if the fit to the sky histogram failed; if a saturated

pixel was within the extraction mask; or if a known bad pixel was within the mask.

One of the advantages of the optimal extraction is that the error estimate is very robust. However, if we compare measurements of the same star in different images (see Section 7) we find that the RMS between measurements never falls below  $\simeq 1$  percent. Such effects are well known in CCD detectors, and probably relate to the intra-pixel sensitivity changes. We shall return to calculating the value of this magnitude independent uncertainty in Section 7, but for the moment simply assume it has a known value.

## 6 PROFILE CORRECTION

Aperture correction is used in classical CCD aperture photometry to correct the flux measured in the small apertures used for the majority of the objects, to the large apertures that must be used for standard stars. In this context the aperture correction is the fraction of the flux which lies outside the small aperture, but inside a large one. Obviously there must be an analogous process for optimal photometry; comparing the flux derived from the optimal photometry, with that in a large aperture. For reasons explained below, we refer to this as the profile correction.

The definition of the profile correction is slightly harder to visualize than that of the aperture correction. As explained in Section 2.3 of Naylor (1998), optimal extraction can be viewed as using each pixel as an independent estimator of the total flux, where the extraction mask gives the fraction of the flux expected in each pixel. Combining these independent estimators in a way that optimises the signal-to-noise ratio is the *raison d’être* of optimal extraction. Even a single pixel, therefore, will give an estimate of the total flux, provided that the mask is a good description of the overall profile. If this were the case, the profile correction would always be zero. In general, however, the mask is only close to the actual profile, and what is encoded in the profile correction is the difference between the true profile, and the extraction mask. Thus if the extraction mask is a perfect match to the observed profile, then the profile correction is zero; non-zero values indicate deviations from this profile.

The difference between an aperture correction and a profile correction can be brought into sharp focus by comparing the effects of the aperture radius used in classical CCD photometry, and the mask clipping radius used in optimal photometry. (This clipping radius, discussed in Section 3.3 of Naylor (1998), is the radius beyond which the optimal extraction mask weights are set to zero, to avoid the masks extending out to infinity.) As the aperture radius grows, and approaches the radius used for the standard stars, the aperture correction tends to zero. Conversely, as the clipping radius grows, there is no change in the profile correction – providing that the extraction mask is a good model of the PSF.

### 6.1 The spatially invariant case

The simplest way to perform this correction is to measure a selection of stars with both the large aperture and the optimal technique, and take the modal value for the difference

between these measurements as the correction. The modal correction is chosen since some stars will have other stars within the large aperture, thus skewing the mean away from the required value. In practice we find that for reasonable aperture sizes, in open cluster fields, even the mode is systematically dragged. We have found a more robust method is to extract sub-images centered on bright stars from the CCD image. We then “median stack” several of these sub-images to create an observed PSF, from which the profile correction can be calculated. If there are other stars within the large aperture of any of the sub-images, the median stacking process ensures their removal.

The details of this method are as follows. We select 80 stars and measure the sky for each one (making sure the uncertainty in the sky measurement does not contribute significantly to the uncertainty in the large aperture flux measurement). We then create a sky subtracted image of each star, normalized such that the flux measured in the optimal mask is the same for each star. If the center of each star lay at (say) the center of a pixel, one could now create a median image, but in practice the center of each star can be at any position within the central pixel. We therefore begin with the brightest star, and re-sample all the other stars onto its pixel gridding, before creating the median stacked image. This works well in the outer regions of the profile, but at the image center, where the gradient of the profile is changing most rapidly, the interpolation tends to smooth the profile. Within this region, therefore, we simply set the pixel values to those of the brightest star. We then repeat this process, creating median images based on successively fainter stars.

It is important to note that the stellarity test has ensured that within the region where median stacking is no longer used (a radius of less than four-thirds of the FWHM), none of the stars chosen are significantly contaminated by another star. Each image should, therefore, produce a reliable profile correction. We normally use the median of the images resulting from the 20 brightest stars, and use the standard deviation as an estimate of the uncertainty in the profile correction.

### 6.2 The spatially variant case

If the point spread function is itself a function of position, then the profile correction must also be supplied as a function of position. The obvious generalization of the above procedure is to divide the CCD into small areas, generate a profile correction for each of them, and then interpolate the correction. In practice such a procedure will run out of bright stars, and so is impractical. Fortunately, the fields where we have encountered a spatially variant PSF, are also sufficiently uncrowded that we can revert to using the profile corrections calculated for individual stars as outlined at the beginning of Section 6.1. We then fit the corrections with a low-order two-dimensional polynomial (after adding the magnitude independent uncertainty derived in Section 7), applying a clipping procedure to remove those objects where the presence of a star in the large aperture gives an anomalous correction. This effect can be seen in Fig. 3, where the upper panels show the profile corrections as a function of X and Y position, and the lower panels show the residuals from the polynomial fit. The objects in the lower panels which lie

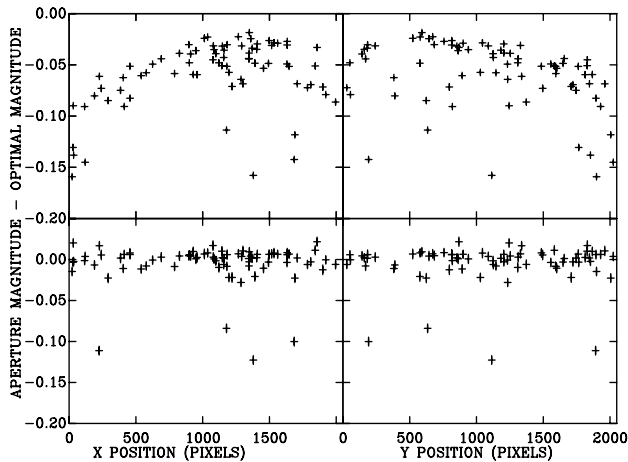


**Figure 3.** The profile corrections as a function of position (upper panels) and their residuals from a two-dimensional polynomial fit which has four terms in each direction, plus a constant (lower panels). The error bars are dominated by the magnitude independent uncertainty (0.005 mags). In the fit for the lower panels 5 data points were zero weighted, yielding a  $\chi^2_\nu$  of 3.4 and an RMS of 10 milli-mags.

below the polynomial fit are those which have other stars within their large apertures, and have been zero weighted.

Interestingly, we do not always obtain the best results by applying the above method in its purest form. Sometimes using the method outlined in Section 6.1 on stars taken from the central region of the CCD, is a better way of setting the constant in the polynomial. The way to decide which method is the correct one to use, is look at the stars in common between CCD images which overlap, and examine how closely the magnitudes deduced from each field match. Although we only have a limited number of datasets to test the two methods for setting the constant, it appears that the pure polynomial method works best when the profile correction is a strong function of position. Presumably this is because the profile correction varies even over the small area used to create the median profile. However, the median profile method is more robust against many faint stars lying within the large aperture, and so works well if the profile is only a slowly varying function of position.

For the NGC2547 V-band data, we found the RMS scatter between fields (before the correction procedure described in Section 9) fell from 0.045 mags to 0.022 mags on changing from using the median profile to the pure polynomial. The details of how this number was derived are discussed in Section 9, however it clearly indicates that the pure polynomial method was the correct one to use for these data.

## 7 COMBINING MEASUREMENTS

The data are dealt with in groups of exposures of the same field taken at similar airmass. The raw counts from the optimal extraction routine are first converted into instrumental magnitudes. For measurements with negative counts we use the modulus of the count rate, and, if the flag is currently

zero, set it to a particular value. This procedure not only preserves the information for objects with negative fluxes, but also means the calibration steps involving adding a correction in magnitude space have the correct effect. The profile correction is then applied, the data are corrected to the mean airmass of the group (using the photometric co-efficients derived in Section 2), and then exposures in the same filter are compared. We arbitrarily assign one frame as a master, and compare each frame with the master, calculating the magnitude differences for all the stars with flags of zero that the two frames have in common. After adding the magnitude independent uncertainty derived later in this section, we take a weighted mean to find the relative transparency correction between this frame and the master.

Where there are  $N$  frames, each frame is corrected by  $N/(N + 1)$  of its relative transparency correction with respect to the master, and the master is corrected by the sum of the transparency corrections divided by  $N$ . Clearly, images taken in non-photometric conditions (such as the short exposures in our wide survey) can be corrected to match the photometric data in a similar way. This process not only improves the internal consistency of the catalogue, but results in an averaging of the profile corrections, improving the absolute accuracy. The transparency corrections derived should be small, and are a test of how accurate the profile correction is, and how photometric the conditions were. The RMS of the transparency corrections applied for the deep survey is about 1 milli-mag, despite the fact that there was some variation in the extinction on the night on which they were taken.

We can now combine the repeated measurements of each star in a given filter and at the same time check that our uncertainty estimates are correct. The observations of an individual star are combined using a weighted mean (in flux space), and at the same time a  $\chi^2$  is calculated. Fig. 4 shows an example of these  $\chi^2$ s as a function of the signal-to-noise ratio in the combined measurement, ignoring the magnitude independent uncertainty. At signal-to-noise ratios of less than a hundred this plot matches the expected distribution of  $\chi^2$  very well, but there is a very clear increase in  $\chi^2$  at high signal-to-noise ratios, implying that we are underestimating the uncertainty. We can now estimate the magnitude independent uncertainty by adding an increasing value in quadrature to the statistical uncertainty, until the distribution in Fig. 4 becomes flat with signal-to-noise ratio. In practice the best way to achieve this is to plot histograms of the distribution of  $\chi^2$  above and below some signal-to-noise ratio cut, and find the value of the magnitude independent uncertainty which makes the two co-incide. Fig. 5 shows the same plot after the completion of this process. We can now create a final weighted mean and uncertainty for each star, which includes the estimated magnitude independent uncertainty for a single measurement.

The reader will no doubt be curious as to the origin of the data creating the feature in the top left of Fig. 5. These are due to weak cosmic ray events. As they appear in just one of the images, they result in a high  $\chi^2$  for the star. Stronger events have a higher  $\chi^2$  and an apparently higher signal-to-noise ratio, hence the feature moves from bottom left to top right. It stops at the point at which the signal-to-noise ratio in the image is sufficiently high that the procedure outlined in Section 4 can be sure they are non

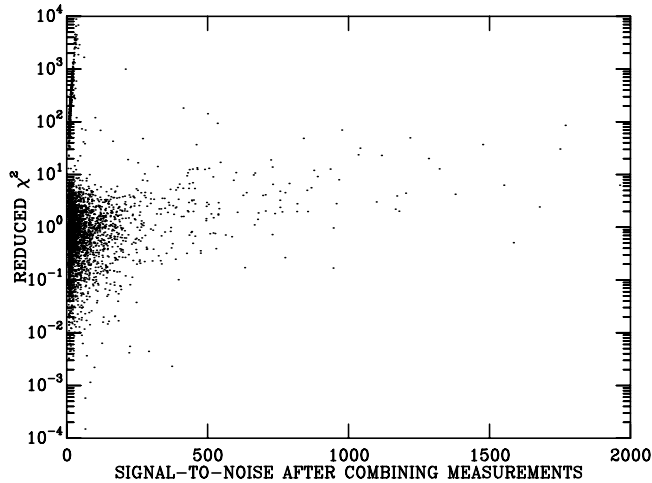


**Figure 4.** The  $\chi^2_\nu$  for each star in the three V-band exposures of deep field 1. The number of degrees of freedom used was two.

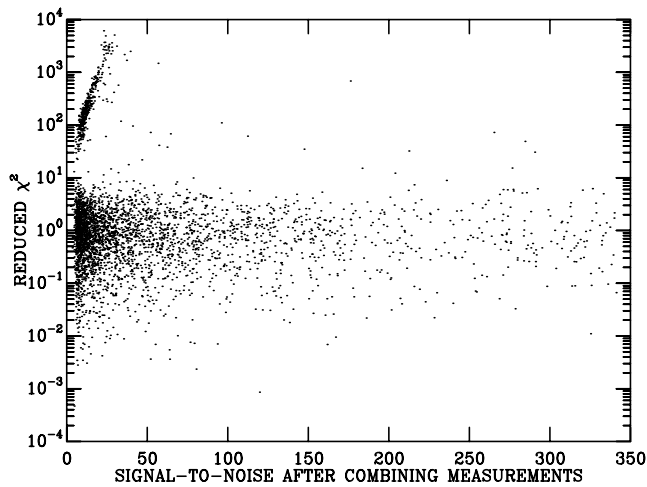


**Figure 5.** As Fig. 4 but after the addition of a magnitude independent uncertainty of 5 milli-mags. Note that this has the effect of reducing the calculated signal-to-noise ratio for the brightest stars.

stellar. For obvious reasons this feature only appears in the  $\chi^2$  plots for the waveband in which the detection algorithm was run.

It is clear that these spurious sources should have non-zero flags in the final catalogue. The simplest way to achieve this is to flag all points with  $\chi^2_\nu$  above some critical value (we use  $\chi^2_\nu > 10$  for the deep fields, 20 for the shallow ones). However, in addition to spurious sources, this will also pick out variable stars, hence we refer to this as the variability flag. As it is uncertain where a variable object should be placed on a colour-magnitude diagram, these stars, like all other objects with non-zero flags are not plotted on our standard CMDs, or included in our later analysis. (Despite the fact that pre-main sequence (PMS) stars are known to be variable, only 3 objects flagged as variable lay close to our PMS. This apparent lack of variability is probably because

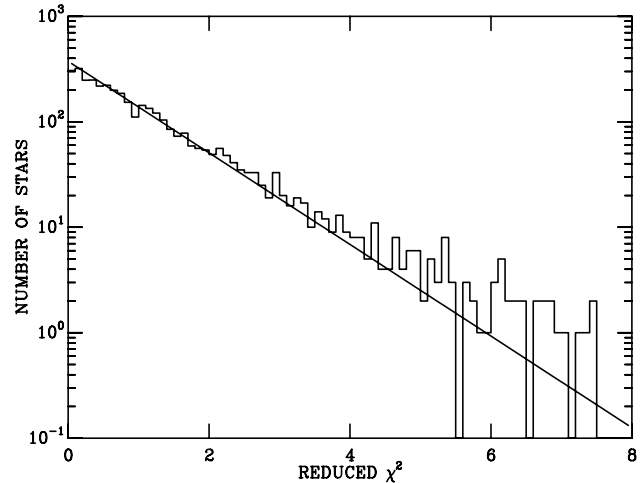


**Figure 6.** The histogram shows the distribution of  $\chi^2$  for each star in the three I-band exposures of deep field 1. The line is the expected distribution of  $\chi^2$  for two degrees of freedom. We emphasize that this is not a fit to the data (there are no free parameters).

when we have repeat images of the same field to the same depth, they are only minutes apart.) It should be noted, however, that this is a very powerful way of detecting variable stars. It is more robust than the standard method of comparing the RMS scatter of a given object with ones of similar magnitude. For example the RMS technique relies on the measurements at different epochs having similar uncertainties, whereas the  $\chi^2$  method works with images of very different effective exposure times.

We should emphasize that the reason we can use  $\chi^2$ , is that the optimal extraction provides very robust error estimates. The data in Fig. 5 allow us to test this, by comparing the distribution of  $\chi^2$  for the stars, with that expected if the uncertainties have been correctly calculated. Fig. 6 shows that the measured  $\chi^2$  distribution matches the theoretical one well. Even recognizing there is a small excess of sources with high  $\chi^2$  (which could be genuine variability), the result is clearly better than the only similar experiment we know of for profile fitting photometry (Caldwell et al. 1991, Fig. 3).

A few of our variable objects will be objects where an instrumental problem, such as a “cosmic ray” has affected a single measurement. With only three measurements we would be uncomfortable rejecting one discrepant point and presenting the mean of the other two as a measurement of a varying object. However, it is clear that given a few more frames, such a strategy may be useful. In the case of the current dataset, we have to rely on the assumption that such events occur randomly across the field, and so the number of stars lost to false variability will be accurately modeled by our completeness correction.

After the  $\chi^2$  testing, the weighted mean instrumental magnitudes for each filter were combined to give instrumental colours on a field-by-field basis. Since each instrumental colour originates from two mean instrumental magnitudes, it has two flags associated with it. As these are one digit integers, the combined flag is defined as ten times the blue



flag plus the red flag. The colours and magnitudes were then transformed onto the standard system using the photometric transformations whose derivation is described in Section 2. Since the transformation for the  $V$  magnitude involves a term in  $B - V$ , it too acquires a two digit flag.

## 8 ASTROMETRIC CALIBRATION

The astrometry is performed using a model with six free parameters to transform pixel co-ordinates into right ascension and declination. We use the SLALIB routines (Wallace 1999) to implement the method outlined in Wallace (1998). This gives us the flexibility to include pin cushion/barrel distortion in datasets where it is required, though a straightforward tangent plane geometry was sufficient for the data presented here. To fix the co-efficients of the model, we need a network of astrometric standards which provides at least tens of stars per CCD field. None of the catalogues of primary astrometric standards provide such a network, but there are several catalogues of secondary astrometric standards which have sufficiently dense coverage for our purposes. We have used both the USNO-A2 (Monet 1998) and 2MASS catalogues for this work, but where it is available (as in the case of NGC2547), we prefer to use the SuperCOSMOS Sky Survey (SSS; Hambly et al. 2001; Hambly et al. 2001). Its primary advantage over the other catalogues is the presence of proper motion information, which we use to update the positions to the epoch of our CCD images. We use the information as to whether stars are part of a blended image to select isolated objects (Blend=0). By default the catalogues supplied from the SSS do not include objects near bright stars. In the case of NGC2547, such a restriction leads to large areas which contain no stars and so we have chosen to accept such objects by accepting SuperCOSMOS quality flags less than or equal to 2047.

We find an initial astrometric solution for each CCD using the positions of three stars. We then use this to pair SSS stars with objects in our fields, and then refine the solution using  $3\text{-}\sigma$  clipping. In the case of NGC2547 the RMS residuals for each field were in the range 0.17-0.20 arcsec for a few hundred stars.

## 9 FINAL PHOTOMETRIC CALIBRATION

Once we have measurements of stars in the standard photometric system, with celestial co-ordinates, we can compare measurements of stars which occur in two or more fields. We calculated the mean magnitude differences in each overlap region for such stars, and then adjusted the zero points for each field to minimize these differences. (Given the interlocking nature of the grid of fields these differences can only be minimized, not entirely removed.) Not only does this process improve the consistency between fields in the final catalogue, but the RMS which remains after this process gives us an estimate of systematic errors with position in the profile correction. In this process we ensured that the mean shift of the nine wide survey fields was zero, since their photometric calibration was tied to their deep exposures, which were taken under photometric conditions. After the adjustment process, the mean differences for the 42 overlaps

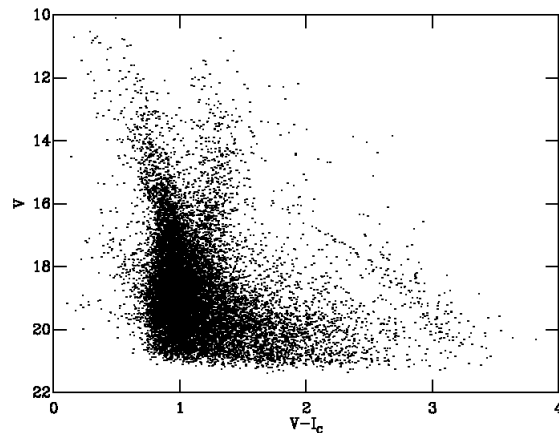


**Figure 7.**  $V$  vs.  $V - I_c$  for the combined catalogue. Sources with a signal-to-noise ratio worse than 10 have been omitted.

in the combined dataset were  $V=0.014$ ,  $B - V=0.005$  and  $V - I_c=0.011$ .

The uncertainties which appear in the catalogue are those calculated at the end of Section 7. It is important that we are clear that this uncertainty represents the scatter between measurements that would be expected were the same field observed repeatedly. They do not include any systematic position-dependent errors in our profile correction. For example, if we used too few terms to represent the profile correction as a function of position, then (assuming the seeing remained the same) it would be systematically wrong in the same sense in every frame. Thus the uncertainty in the catalogue should be used to compare the magnitudes of stars at similar positions in the field. If one wishes to compare stars at, say, opposite sides of the field, or from different fields, then one must add the error derived from the overlap between fields. Finally, if one wishes to compare our photometry with other work, the uncertainty in our photometric calibration should be added.

## 10 THE FINAL CATALOGUES

Given the different depths of the two surveys, it was found useful to keep three separate catalogues, one for the four deep fields, one for the nine fields of the wide survey, and one which is the result of combining all 13 fields. We will refer to these as the deep, wide and combined catalogues respectively. (Note that the corrections derived from the overlaps and applied to each field are, in all cases, those derived from combining all the fields.) The wide and combined catalogues cover approximately 0.32 square degree, the deep catalogue 0.12 square degree. In Figs. 7 to 9 we show CMDs from these catalogues, restricted to stars which have flags of zero in each co-ordinate. In Table 2 we present an example catalogue, which is the stars in common between the combined catalogue and Clariá (1982). We choose this as our example as it allows easy cross identification between our own work and that of Clariá, which would otherwise be difficult as there are only finding charts, not positions in Clariá (1982).

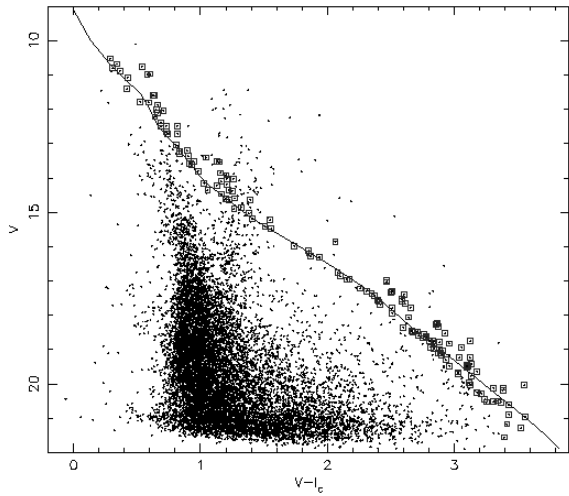


**Figure 8.**  $V$  vs.  $V - I_c$  for the enhanced deep catalogue. The solid line is the best fitting D'Antona & Mazzitelli isochrone discussed in Section 11 and the points enclosed by squares are candidate cluster members selected in Section 12. Sources with a signal-to-noise ratio worse than 5 have been omitted.

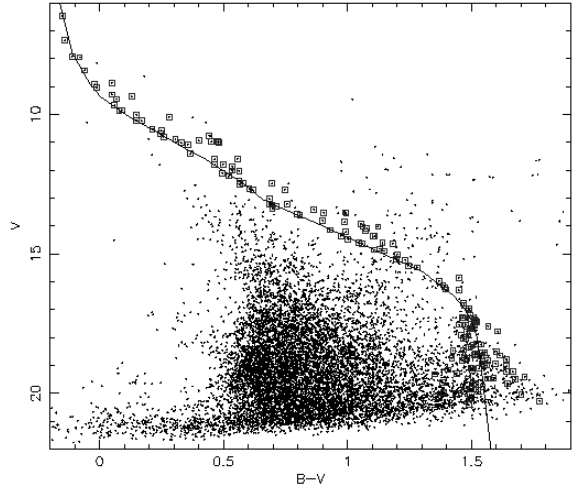


**Figure 10.**  $V$  vs.  $B - V$  for the enhanced deep catalogue. The solid line is the best fitting D'Antona & Mazzitelli isochrone discussed in Section 11 and the points enclosed by squares are candidate cluster members selected in Section 12. Sources with a signal-to-noise ratio worse than 5 have been omitted.

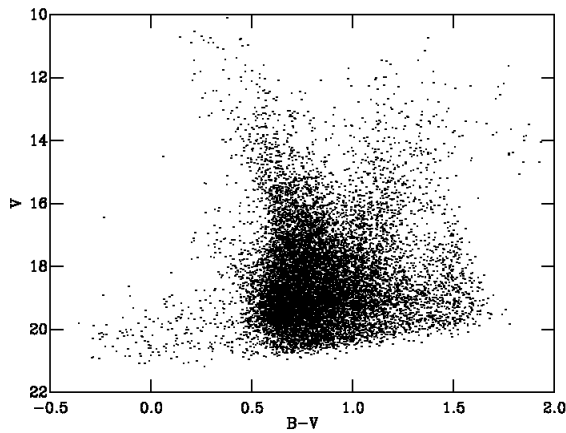


**Figure 9.**  $V$  vs.  $B - V$  for the combined catalogue. Sources with a signal-to-noise ratio worse than 10 have been omitted.

In magnitude space, the error bars for an object are two sided. We have chosen to quote those for the bright side of the data point for the following reason. It is desirable that the bright side error bar for objects with positive fluxes matches smoothly onto the upper limit for objects with zero flux. For this to be true it means that as the flux for an object tends to zero, the result of subtracting the magnitude uncertainty from the magnitude (i.e. calculating the bright end of the error bar) must tend towards the value obtained by converting the flux uncertainty into a magnitude. This forces our choice of the bright-side error bar. However, for situations where the faint side error bar is important, it is trivial to show that it can be calculated from the uncertainty we give ( $E$ ) as

$$-2.5 \log_{10}(1 - (10^{E/2.5} - 1)^2). \quad (1)$$

Since the deep survey did not contain data for the brighter stars, we obtained this from both the wide survey and the data of Clariá (1982) in the following way. We first extracted the saturated stars from the deep catalogue, and then searched at these positions for stars in the wide survey. Where magnitudes with flags of zero were found, these were inserted into the deep catalogue, and the stars deleted from our list of saturated objects. We then searched Clariá's catalogue for counterparts for the remaining objects in our saturated list, and placed these into the deep catalogue as well. We refer to the result of this process as the enhanced deep catalogue. We resisted the temptation to replace entries with the bad pixel flag in the deep catalogue with entries from other catalogues, as this would have made the area of sky surveyed a function of magnitude.

In a similar way we replaced all saturated objects in the wide and combined catalogues with magnitudes from Clariá (1982), to create an enhanced combined catalogue and an enhanced wide catalogue. It should be remembered that Clariá (1982) only contains data in  $V$  and  $B - V$ , and thus the enhanced catalogues reach brighter magnitudes in  $V$  and  $B - V$  than  $V - I_c$ . The enhanced deep, wide and combined catalogues have been deposited with Centre de Données astronomiques de Strasbourg as Tables 3, 4 and 5 respectively. They contain all the columns of Table 2, except for the Clariá identification numbers.

One striking feature of the  $V, B - V$  CMDs is the appearance of faint blue objects. Since similar objects also appear in the wide catalogue, but at slightly brighter magnitudes, they are clearly spurious. Indeed, comparison of Figs. 9 and 10, show how there are many more such objects at lower signal-to-noise ratios. Close examination shows that these spurious objects are often associated with bright stars, which are so faint that they cannot reliably be classified as non-stellar. The fact they appear blue is presumably related to the nature of the scattering in the optics which produces them. These objects produce a sharp increase in the num-

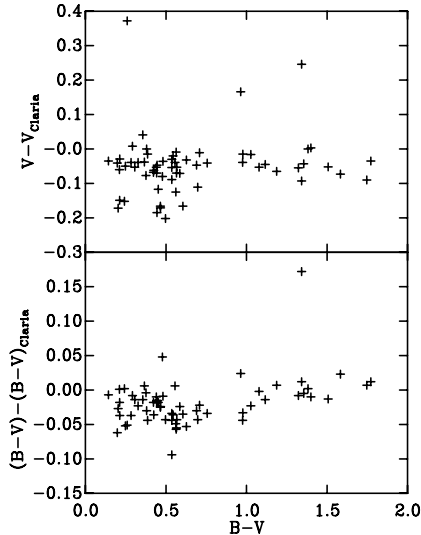


**Figure 11.** The difference between the  $V$  magnitudes and  $B - V$  colours we derived and those of Clariá, as a function of our  $B - V$ . Although the  $B - V$  differences appear to be a function of colour, a linear term is only significant at the 73% level.

ber of objects which appear in the wide catalogue, but not in the deep catalogue (and are therefore spurious), below  $V=20.0$ , or an uncertainty of 0.08 mags. Approximately 30 percent of objects below this limit are spurious. However, as the corresponding point in signal-to-noise ratio in the deep catalogue is  $V=20.7$ , this can only affect the last bin of our mass function derived in Section 15, and the largest possible effect is less than the error bar.

### 10.1 Comparison with previous work

The best comparison we can undertake is with the photoelectric photometry of Clariá (1982) since, in the magnitude range in question, the uncertainties in both our own and Clariá's photometry are independent of magnitude. Of 118 stars in Clariá (1982) between  $V=5.6$  and  $V=13.98$ , 102 lie within the area of the combined catalogue, and all are detected. Of these objects a total of 39 were some combination of saturated, lying on bad pixels or non-stellar. The remaining objects are plotted in Fig. 11. Three have large differences between the two catalogues which can be attributed to nearby companions in each case. This leaves 60 objects for comparison. In  $B - V$  we find a RMS difference of 0.024 mags, and an (unweighted) mean difference  $(B - V) - (B - V)_{Claria} = -0.021$  mags. The RMS difference is acceptable as the uncertainty in an individual star's magnitude is dominated by the profile correction (0.005 mags, Section 9, though in some cases the statistical uncertainty reaches 0.02 mags) in our data, and is about 0.02 mags in the photoelectric work (Clariá 1982). The mean difference is acceptable as the combination of the uncertainties in the photometric calibration of the two datasets.

There appears to be a problem with the  $V$  comparison, in that eight of the remaining 60 objects form a group which appear about 0.1 magnitudes brighter in our data than Clariá's. Although seven of the eight stars are on our field 18, this is clearly not a problem with that field, as two of the eight stars appear on other fields, and the dif-

ferences between the two measurements are two hundredths or less, and within the error bars. Furthermore, if we examine the region of the PMS where it is best defined, around  $V - I_c = 2$ , shifting field 18 by 0.1 magnitudes makes the PMS members in that field lie above those in the rest of the catalogue. We conclude that the Clariá (1982) measurements are incorrect, but do so reluctantly as there is not an obvious reason why this should be so. Removing these outliers we find an RMS difference of 0.032 mags and an average difference of  $V - V_{Claria} = -0.047$  mags. Again the RMS is acceptable as the sum of our profile correction of 0.014 mags, and Clariá (1982)'s estimated uncertainty of 0.02 mags. The mean difference in  $V$  is disturbing, but is similar in magnitude (though opposite in sign) to the difference between photoelectric photometry and modern CCD photometry found by von Hippel & Sarajedini (1998) for NGC188.

It is also important to note that there is an almost one-to-one correspondence between saturated objects in our catalogues and objects in the Clariá (1982) photometry. This is because our detection algorithm does not break single saturated stars into multiple objects. The only problem is that the derived position for a few very badly saturated objects (some are 10,000 times above our saturation limit) is sometimes much worse than the 1.5 arcsec correlation radius we use for identifying the same object observed in two or more fields. Fortunately such objects are easy to identify, as they are very bright stars at similar positions but in two separate fields. This one-to-one correspondence is crucial, since it means we can be confident we have a complete count of all objects, even though they may be saturated in our data.

Fig. 12 shows the comparison between our combined catalogue and the results of Jeffries & Tolley (1998). The interest of this comparison is that Jeffries & Tolley (1998) used the same data, but reduced by more conventional (aperture photometry) algorithms. Here, we reach sufficiently faint magnitudes that the error bars are significantly different for some stars, and thus use weighted mean differences. In addition we remove some outliers. We find a mean difference of  $(V - I_c) - (V - I_c)_{JT} = -0.009$ . The behaviour for  $V$  and  $B - V$  is more complex.  $V - V_{JT} = -0.011$  for  $V < 17$ , but thereafter  $V - V_{JT}$  falls linearly, reaching about -0.15 at  $V=19$ . Similarly,  $(B - V) - (B - V)_{JT} = -0.012$  for  $B - V < 1.33$ , but then falls to -0.25 by  $B - V=1.8$ . The Jeffries & Tolley (1998) stars are mainly along the pre-main-sequence, and thus  $V$  is strongly correlated with  $B - V$ , so it is difficult to be certain whether the above correlations are with  $V$  or  $B - V$ , however, they are tightest in the forms stated above.

Perhaps most the important comparison is that of the signal-to-noise ratio achieved in our reduction, and that of Jeffries & Tolley (1998). For a  $V=19$  star which appears in just one of the longer exposures of the wide survey Jeffries & Tolley (1998) give an uncertainty of about 0.06 magnitudes compared with our uncertainty of 0.04 magnitudes; an improvement of 1.5 in signal-to-noise ratio. This means that at a given signal-to-noise ratio, our CMDs reach about 0.45 magnitudes deeper than the aperture photometry.

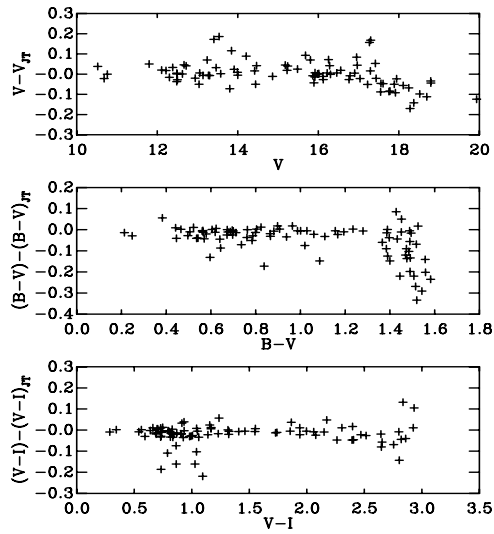


**Figure 12.** The difference between the  $V$  magnitudes and  $B - V$  and  $V - I$  colours we derived and those of Jeffries & Tolley. Between two and four data points lie outside the Y-axis scaling of each panel.

## 11 X-RAY SELECTION, AND THE AGE OF THE CLUSTER

To determine the age of the cluster we fitted an isochrone to the X-ray selected members. This is essentially an updated version of the analysis of Jeffries & Tolley (1998), though with a deeper catalogue. In addition, by repeating the analysis, we ensure that the mass function we will derive in Section 15 is based on an isochrone which is consistent with the new reduction of the photometry. We therefore cross-correlated our enhanced combined catalogue against the X-ray catalogue of Jeffries & Tolley (1998), using the error radius appropriate to each X-ray position. We extracted all the stars within each error circle, and noted which was the brightest within each circle. The resulting CMDs are shown in Figs. 13 and 14.

There are a small number of sources, which lie close to the PMS, which are not the brightest objects in their error circles. As this could be either a sign that the PMS stars are spatially clustered, or that a brighter non-member appears in the error circles by chance, we examined the five such objects fainter than  $V=18.5$  close to or above the PMS. Three objects have brighter stars in their error circles which are clearly not members, whilst two have brighter PMS objects in their error circles. To establish if the latter are consistent with a random distribution of sources on the sky, we tried shifting the error circles by  $\pm 30$  and 60 arcseconds in declination. In these randomly placed error circles, we found an average total of 0.5 sources in each of our four simulated datasets at positions in the CMD consistent with the PMS. Although 0.5 is rather different from two, they are consistent within the uncertainties, establishing that there is no clustering of the PMS stars.

With this issue clarified, we then began fitting the X-ray selected members. The methods that we use to generate model isochrones to fit the colour-magnitude diagrams are described in great detail by Jeffries et al. (2001). Briefly, we generate a set of model isochrones based upon the so-

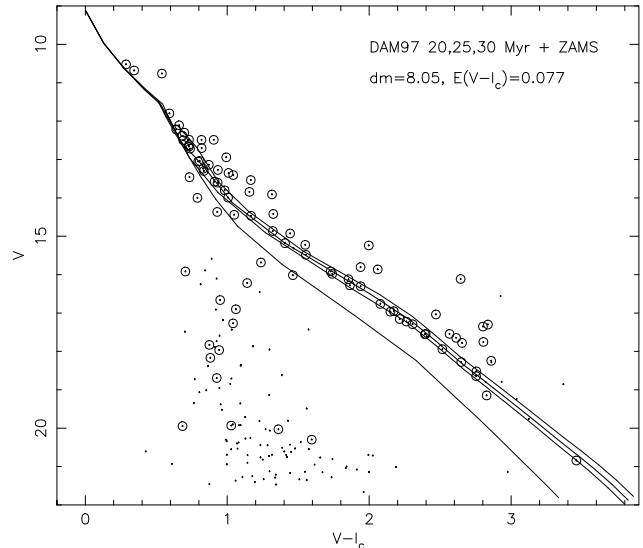


**Figure 13.** The CMD for the stars in the enhanced combined catalogue within X-ray error circles. Every star in an X-ray error circle is marked with a dot, with the dot for the brightest object within an error circle, circled. The solid lines are isochrones derived from the models of D’Antona & Mazzitelli (1997).

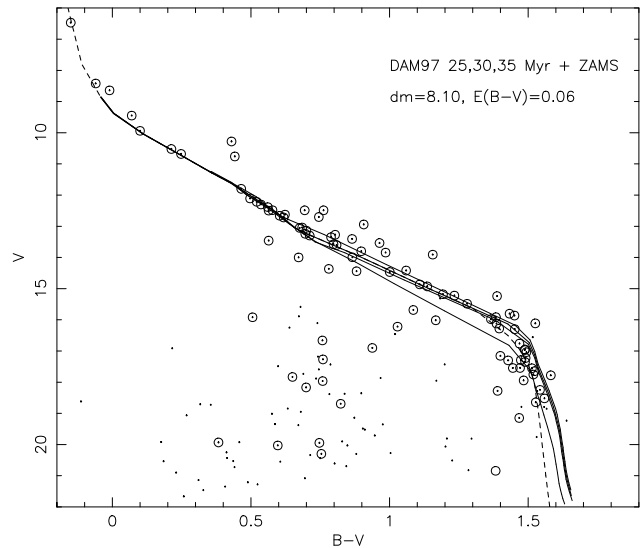


**Figure 14.** As for Fig. 13, but in  $V$  vs  $B - V$ . The brighter members do not appear in Fig. 13 as they lack  $I$ -band photometry. The solid lines are isochrones derived from the models of D’Antona & Mazzitelli (1997). The dashed lines show the extensions and alterations to the 30 Myr isochrone that have been used to select candidate members in Section 12 (see Section 11).

lar metallicity models of D’Antona & Mazzitelli (1997) and Siess et al. (2000). These models cover *most* of the mass range required to interpret our NGC 2547 data, although the D’Antona & Mazzitelli models are limited to  $3M_{\odot}$  at the high mass end. These isochrones are converted into the observational colour-magnitude plane, using empirical  $T_{\text{eff}}$  to colour conversions, derived by assuming that the Pleiades defines an isochrone at an age of 120 Myr and distance of 130 pc (Stauffer et al. 1998). Note that if a different fiducial distance were adopted for the Pleiades, this would change our derived distance for NGC 2547 by a similar percentage. In addition we need to assume relationships between bol-

metric correction and colour, which come from Flower (1996) for  $B - V$ , Leggett et al. (1996) for  $V - I_c > 0.7$  and the atmospheric models of Bessell et al. (1998) for  $V - I_c < 0.7$ .

These isochrones are then compared to the objects which correlate with X-ray sources. As discussed by Jeffries & Tolley (1998), these are very likely to be cluster members with very little contamination by non-members, so should allow us to determine the cluster age, distance and reddening. For the purposes of this paper we choose to fix the reddening at the value of  $E(B - V) = 0.06$ , determined from the hot stars by Clariá (1982). We further assume a standard reddening law and that  $E(V - I_c) = 0.077$ . Having done this, we find that the age and distance are only partially degenerate parameters. The distance is reasonably well determined from the hotter ZAMS stars, especially in the  $V$  vs  $B - V$  diagram, whereas the age is determined by the positions of the cooler stars which are still descending PMS tracks towards the ZAMS. Any effort to find the best-fit age and distance, by minimising chi-squared for example, is fraught with difficulty, because many of the X-ray sources appear to be either non-members, or are binary members of the cluster and lie above any single star isochrone. However, by eye, there does appear to be a clear sequence of about 30 stars in each CMD which we assume defines the cluster single star isochrone. We proceed by choosing isochrones of different ages and then adjusting the distance modulus to get what appears to be the best possible fit to this sequence. The uncertainties of this process are mostly due to the degeneracy between distance and age, but because the isochrones change *shape* with age, we find that beyond certain limits we cannot adjust the distance and get a reasonable match between the data and the model.

The best fitting D'Antona & Mazzitelli (1997) models are shown in Figs. 13 and 14. For  $V$  vs  $B - V$  diagram we find an intrinsic distance modulus of  $8.10 \pm 0.05$  and an age of  $30 \pm 5$  Myr. For the  $V$  vs  $V - I_c$  diagram we find an intrinsic distance modulus of  $8.05 \pm 0.10$  and an age of  $25 \pm 5$  Myr. The Siess et al. (2000) isochrones are similar but we find ages approximately 5 Myr older. That the distance modulus in the  $V$  vs  $B - V$  CMD may be slightly larger than for the  $V$  vs  $V - I_c$  CMD, might be attributable to a slightly subsolar ( $[\text{Fe}/\text{H}] \sim -0.1$ ) metallicity for NGC 2547 (see Jeffries et al. 2001, for discussion). If this were the case the intrinsic distance modulus would be lowered to 7.95-8.0. Either range of distances is consistent with that derived from the Hipparcos data of  $8.18_{-0.26}^{+0.29}$  (Robichon et al. 1999). To illustrate the validity of our uncertainty estimates, Figs. 15 and 16 show our best efforts to obtain fits at both younger (15 Myr) and older (40 Myr) ages, using the D'Antona & Mazzitelli (1997) models. The younger age is ruled out using the  $V$  vs  $V - I_c$  CMD. The shape does not really match the observed sequence and the required distance modulus is *much* larger than the  $8.10 \pm 0.05$  defined by the hotter ZAMS stars in the  $V$  vs  $B - V$  CMD. The older age is ruled out by the  $V$  vs  $B - V$  CMD. The stars between  $0.8 < B - V < 1.4$  cannot be simultaneously fit with the higher mass objects that have reached the ZAMS. Thus we conclude the age lies between 20 and 35 Myr, using the D'Antona & Mazzitelli (1997) models.

The value for the distance is similar to that quoted by Jeffries & Tolley (1998), but the age is somewhat older (c.f.  $14 \pm 4$  Myr), even though the same D'Antona & Mazzitelli

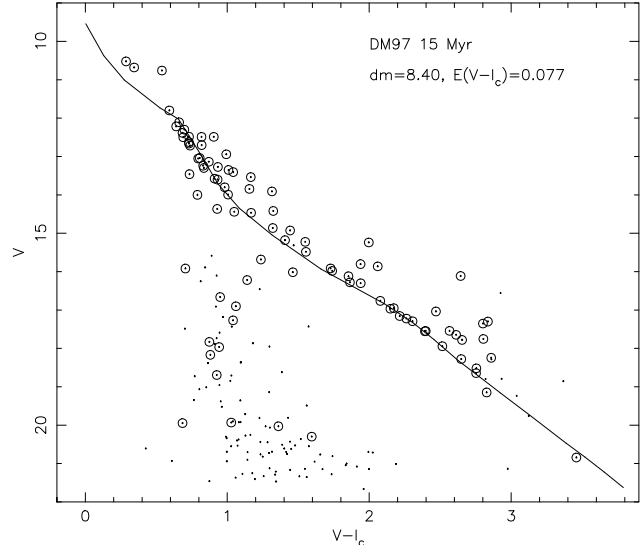


**Figure 15.** As for Fig. 13, but showing the poor fit given by an age of 15 Myr with the models of D'Antona & Mazzitelli (1997).

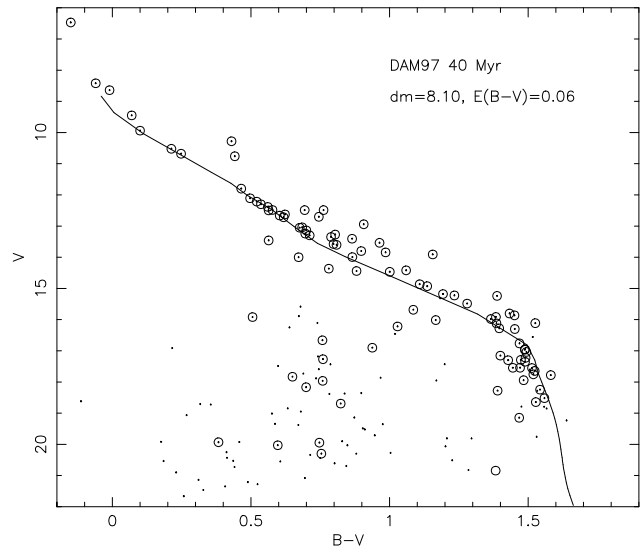


**Figure 16.** As for Fig. 14, but showing the poor fit given by an age of 40 Myr with the models of D'Antona & Mazzitelli (1997).

(1997) evolutionary models are used in that paper. We attribute this difference to the use of a relationship between bolometric correction and  $T_{\text{eff}}$  in Jeffries & Tolley (1998), to convert luminosities to absolute  $V$  magnitudes – a practice commonly found in the literature. The method described above and in Jeffries et al. (2001) uses the *much* more reliable conversion between bolometric correction and *colour*.

We note that the fit of the isochrones in the  $V$  vs  $B - V$  CMD is poor around  $B - V \simeq 1.5$ . This may be a problem with the evolutionary models or a problem in the relative calibration of our photometry with that of the Pleiades used in defining the  $B - V$  effective temperature relation. We note that we have plenty of well measured standards beyond  $B - V = 1.5$  and that our transformation from instrumental to standard  $B - V$  is therefore well constrained. In order to define an isochrone that can be used solely to select cluster candidates we have arbitrarily defined an isochrone that departs from the 30 Myr D'Antona & Mazzitelli isochrone

at  $B - V > 1.35$  and which passes through the bulk of the X-ray sources (see Fig.11). In the same spirit, we have also extended the model isochrone to higher masses.

## 12 SELECTION OF CLUSTER CANDIDATES

### 12.1 Candidate selection

Selection of candidate members of NGC 2547 proceeds exactly in the way described in detail by Jeffries et al. (2001). Each star in the catalogue is tested against a number of criteria for membership. If a star does not fail any of these tests then it is retained as a candidate member. Briefly, these tests consist of investigating whether a star is: (a) close to the  $V$  vs  $V - I_c$  isochrone defined in Sect.11; (b) close to the  $V$  vs  $B - V$  isochrone; (c) close to the  $V - I_c$  vs  $B - V$  locus for cluster members. We reject those measurements which have a non-zero flags or uncertainties of greater than 0.2 mag. A star must have at least a  $V$  magnitude and one measured colour to be classed as a candidate member. In practice, there are some differences in the membership list depending on whether we use the D’Antona & Mazzitelli (1997) or the Siess et al. (2000) isochrones. Despite having distance and age as free parameters, the two sets of evolutionary models give isochrones that have slightly different *shapes*, particularly for the very cool stars.

In addition we apply a final test for possible binarity. If a star lies more than 0.3 mag. above the  $V$  vs  $V - I_c$  isochrone (or the  $V$  vs  $B - V$  isochrone for stars with  $V - I_c < 0.5$ ) we class them as candidate unresolved binary systems. To calculate what mass ratios we are sensitive to, we have used the slopes of our CMDs and mass-magnitude relationships (see Section 15), and equation 5 from (Kähler 1999). We find that  $\Delta V \geq 0.3$  corresponds to a mass ratio  $q \geq 0.6$  for  $V < 14$  and  $q \geq 0.5$  for fainter cluster members. The reason for the difference is the change in slope of the CMDs and mass-magnitude relation as PMS stars reach the ZAMS. In contrast, for older clusters like the Pleiades,  $\Delta V \geq 0.3$  corresponds to  $q \geq 0.6$  over the entire mass range considered here.

The reader might suspect that by choosing only objects flagged as stellar, we may have excluded wide binaries that would appear as non-stellar objects in the catalogue. In fact, given the typical seeing of our data and the distance of the cluster, equal mass binaries would have to be separated by more than a few tenths of an arcsecond (more than 100 AU) and unequal mass binaries by even more. Bouvier et al. (1997) estimate that the fraction of such systems among the intermediate and low-mass stars of the Pleiades is at most a few percent, so it is possible we have rejected these systems as well as triple (or even higher multiple) systems that might fall outside our selection criteria in the colour-magnitude diagrams (estimated as less than 2 percent of systems – Mermilliod et al. 1992). Incompleteness of this order will have no great effect on any of our results or conclusions.

We used the D’Antona & Mazzitelli isochrones to find 184 cluster candidates from our enhanced deep catalogue, of which 52 are probable unresolved, high mass ratio binaries. The Siess et al. (2000) isochrones yield 201 cluster candidates, of which 61 are candidate binaries. The additional

members in the Siess et al. case are mainly at faint magnitudes (see below). Figs. 8 and 10 show the filtered, deep  $V$  vs  $B - V$  and  $V$  vs  $V - I_c$  CMDs, with both the loci used to select the cluster candidates and the selected cluster candidates indicated (for the D’Antona & Mazzitelli isochrones). Tables presenting ID and field numbers (data from Clariá (1982) are given as field zero), equatorial co-ordinates, membership and binary flags have been deposited with Centre de Données astronomiques de Strasbourg as Tables 6 and 7 for D’Antona & Mazzitelli (1997) and Siess et al. (2000) models respectively.

### 12.2 Field star contamination

We are confident that our membership selection criteria have included almost all the true cluster members. However, despite having a cleanly defined sequence, especially in the  $V$  vs  $V - I_c$  colour-magnitude diagram, it is inevitable that we have included contaminating field stars as candidate members. Jeffries et al. (2001) devised a scheme to estimate the size of this contamination (as a function of colour), by interpolating the distribution of background stars over the interval from which cluster candidates were selected. Unfortunately in NGC 2547, there are far fewer stars immediately above and below the cluster sequence with which to do this interpolation, and we find that this technique will not work, apart from in the region where background giants intrude at  $14.0 < V < 15.5$ . The total number of stars in the NGC 2547 catalogues is comparable to those discussed by Jeffries et al. (2001) for NGC 2516, an older cluster ( $\sim 100 - 150$  Myr) at a similar distance. It seems then that the numbers of contaminating field stars in the NGC 2547 must be much lower than for NGC 2516, despite NGC 2547 being at a lower galactic latitude ( $b = -9^\circ$  and  $-16^\circ$  respectively). We believe this is (a) because we have observed a smaller area in NGC 2547 and (b) because NGC 2547 is younger than NGC 2516 and so, at a similar distance, the NGC 2547 isochrone for cool PMS stars lies more than a magnitude above the ZAMS in the colour-magnitude diagram and hence clear of the background contamination.

For the rest of this paper we will make the assumption that contamination of our NGC 2547 cluster sample is negligible. The exception is between  $14.0 < V < 15.5$  where integration of an interpolation of the density of stars above and below the cluster sequence, suggests that there, the field star contamination could be as high as 40 percent. Note that this assumption was recently tested for the brighter stars ( $12 < V < 14$ ) by Jeffries et al. (2000). They performed high resolution spectroscopy of 23 of the stars selected as cluster candidates in this paper. From the radial velocities there is good evidence that at least 20, and probably all, of these stars are cluster members.

## 13 COMPLETENESS – GHOST STARS

Before we can construct a luminosity function from our candidate list we must determine the fraction of stars at a given magnitude which we detect and for which we successfully obtain photometry. Examination of the reduction path shows the following hurdles a PMS star must overcome to appear in our final catalogue. First it must be detected in our V-band

images. Most simply, it may be too faint, but as the point-spread function is a function of position, stars of a given magnitude are less likely to be detected at the frame edges than at its center. It may also not be detected because it lies close to a brighter star, or a chip defect. Next, our test for point-like objects (Section 4) will reject some small proportion of star-like objects. The detected object will next pass through the photometry routines, when, to appear in the final catalogue, it must avoid being flagged for saturation or proximity to chip defects or a CCD edge. Very occasionally a star will also acquire a non-zero flag because the fit to the sky histogram fails. When several measurements of the same object are combined the star may be rejected on the grounds of variability. Finally, a PMS star which appears in our final catalogue, may be rejected because it falls outside our selection strip.

The most convincing way to account for this mass of selection criteria is to inject a simulated sequence of PMS stars into the data and examine what fraction appear in our final catalogue, and are selected as PMS stars. This has the advantage that we simulate our completeness as a function of colour, as well as magnitude. (This is important, not only because of colour terms in the photometric transformation, but also because the error bars in the colours are a function of colour as well as magnitude.) As we have not modeled the PSF as a function of position, we cannot generate stars at random positions on the CCD. Instead we use the following procedure, which we term “ghosting”. The essence of this technique is that images of the brightest stars in the field are sky-subtracted, scaled to the required brightness for a simulated star, and copied to a nearby position. The position has to be sufficiently close that the PSF has not varied significantly, but far enough away to avoid the wings of the original.

### 13.1 The area to be copied

The most significant issue with ghosting is deciding how large an area must be copied. The detection technique relies on the counts within a sliding box being greater than the detection threshold. As long as the total counts in the box lie above the threshold when the box is at the peak of the star, the star will be detected. The wings of the star are irrelevant. Thus for the detection algorithm to work, an area equal to the detection box (typically one FWHM) must be copied. The position of the star is determined by fitting it (see Naylor 1998), and the box used for this is twice the FWHM (corresponding to a “fitting radius” of a FWHM), so again only a small area needs to be copied. For the photometry to be successful, the copied area must cover the weight mask out to the radius at which it is clipped, normally two FWHM. Thus it is the requirements of the photometry which decide the area to be copied, and which normally sets it to two FWHM. If we copy the star out to two FWHM radius, can we be sure that the original is point-like at this radius? The answer must be yes, since otherwise it would have been flagged as non-stellar. Despite the above reasoning, the brighter ghosts can be quite striking in appearance, with a discontinuity at the edge of the copied area. However, this does not affect their detectability, or measured brightness.

### 13.2 Practicalities of the simulation

To create the ghosts, we first create a list of the magnitudes and colours of the stars we wish to simulate. We then select a parent to be used for each ghost, scale it appropriately, and insert it into each image at a given offset from the parent. The most obvious way to decide the scaling is to use the measured photometric transformations to calculate the number of counts required in the ghost. However, a whole series of minor corrections, such as the relative transparency correction (Section 7), have been applied to the data. It is simpler, therefore (and hence more robust against coding errors) to subtract the required magnitude from that given for the parent in the final catalogue, and use the colour transforms to allow for any differences in instrumental magnitude introduced by both stars’ colours.

If we simply added the scaled, sky subtracted parent to the image at the position of the required ghost the final image would not have the correct noise properties. For example, the noise in the wings of the ghost should correspond to the noise in the sky at this point, and so the addition of a noiseless parent would have the correct effect. However, the parents are never noiseless, and so without some further procedure one would always have too much noise in the ghosts’ wings. Before adding the ghost, therefore, we replace each pixel in the area with the median of itself and the eight pixels around it, removing the majority of the sky noise. We then calculate the noise required in the ghost, subtract from it the noise already present in the scaled parent, and then perturb the final image by this amount. This, of course, requires that the parents are always considerably brighter than the ghosts. The median process will also slightly broaden any star the ghost lies close to, but this should not affect our completeness calculation.

It is important that we correctly simulate stars which lie in overlap areas between two or more fields. Their multiple measurements are averaged, resulting in a higher signal-to-noise ratio for a given magnitude, which can affect any completeness which includes a signal-to-noise ratio cutoff. Our creation of the ghost and parent list is therefore carried out from the final catalogue. The celestial co-ordinates of every star are then translated back to pixel co-ordinates for every image, and the star inserted if it lies on the image. The only potential problem here would be if a ghost lay on an image, but not its parent. To ensure this does not happen, the positional shift from parent to ghost is always parallel to the closest CCD edge and towards the middle of that edge.

Once the simulated stars have been introduced into each image of a given field, it is straightforward to run these images through the entire data reduction process. In practice it is much faster to carry out only photometry of the stars which have been injected into the images. Thus, after the star detection algorithm has run, we select those stars which lie close to the position of ghosts, and only carry out photometry of these objects.

### 13.3 Testing the technique

We can use the area of the wide catalogue which is covered by the deep catalogue to *measure* the completeness function for the wide catalogue, and then compare it with the *prediction* made by our completeness correction. Although

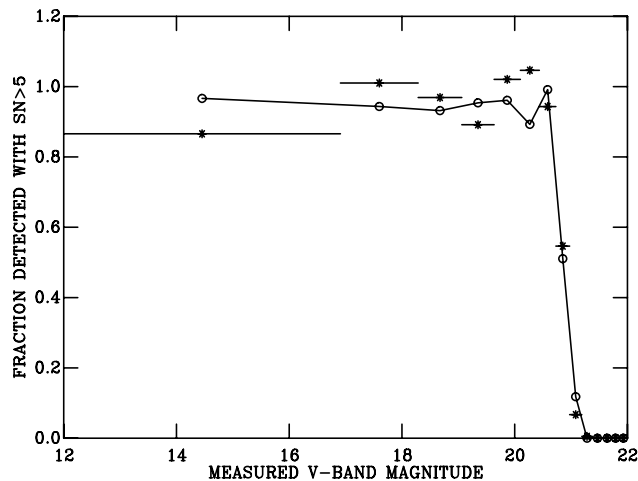


**Figure 17.** The completeness function (including magnitude creep) for the area of the wide survey which overlaps with the deep survey. The measured completeness function is the line with circles, that predicted by simulation is marked as bars with stars. The magnitude bins for the two datasets are identical, and shown by the bars on the starred points.

such a test is clearly crucial to validating any correction, we are unaware of similar experiments being carried out to test other techniques.

In principle, to measure the completeness of the wide catalogue, one simply takes each star in the deep catalogue, and asks whether it was detected in the wide survey. In practice, we know colour effects are important, so we began by selecting just those objects in the deep catalogue with colours  $0.95 < V - I_c < 1.25$ . We then searched for stars with matching positions in the wide catalogue, which also had flags of zero, and a signal-to-noise ratio greater than five. The fraction of deep catalogue objects which appear in the wide catalogue and pass the above tests, is our measured completeness function. It is plotted as a circled line in Fig. 17.

We matched this by simulating, in the wide survey, a sequence with  $V - I_c = 1.1$  and  $B - V = 0.7$  (the  $B - V$  is close to the mean for the dataset). We increased the number of stars in the sequence exponentially with magnitude, so that the number per magnitude increases by a factor 1.71 per magnitude; similar to the increase with magnitude for the entire catalogue. We took the ratio of detected simulated objects with flags of zero and a signal-to-noise ratio greater than five, to input objects. The result as, a function of detected magnitude, is our predicted completeness function for the wide survey, plotted as stars in Fig. 17.

Fig. 17 shows a remarkable degree of agreement between the predictions of our simulations, and the actual completeness function. Equally encouraging, the detection efficiency falls from 90 to 10 percent in about half a magnitude. Such a sharp cut-off is highly desirable for constructing luminosity functions, since it limits the region affected by (possibly) inaccurate completeness corrections. Finally we note that sometimes the completeness correction is greater than one. This “magnitude creep” is caused by objects being detected in a magnitude bin other than that which they were simu-

lated, either because of statistical uncertainty or the presence of another star (see Stetson 1991). In practice the nett effect of magnitude creep is to place too many stars in the brighter bins, but the effect depends on the slope of the luminosity function, so it is important the simulated one chosen is close to that of the data. There is a further reason for matching the slope of the luminosity function in the simulations. The completeness function is presented in bins where, close to the cut-off, both the luminosity function and the completeness function vary significantly within the binning. As long as the real and simulated luminosity function are similar, binned data will be directly comparable.

#### 14 THE CLUSTER LUMINOSITY FUNCTION

The objects selected as cluster candidates are placed into  $V$  magnitude bins and plotted in Fig. 18 as the cluster luminosity function. The technique described in Section 13 was used to estimate the correction for completeness. A simulated PMS was used which matched the colours of the fitted PMS, with a similar growth in number with magnitude. The derived correction by which the number of sources must be divided ( $C$ ) was fitted with a function of the form

$$C = B - Ae^{\frac{m-O}{W}}, \quad (2)$$

where  $A$ ,  $B$ ,  $O$  and  $W$  are constants, and  $m$  is the magnitude referred to. Although in principle this correction can become negative, in practice our there are no sources with an implied correction less than or equal to zero. This correction was applied on a star-by-star basis before binning, so that each star contributes a little more than 1 to the bin that it is placed in. Both corrected and uncorrected luminosity functions are shown for comparison, as well as corrected luminosity functions based on both the D’Antona & Mazzitelli and the Siess et al. isochrones. In Fig. 18, the x-axis has been transformed to absolute  $V$  magnitude by subtracting 8.25 (distance plus extinction) from the observed magnitudes.

We believe that there is strong evidence for a turnover in the luminosity function for  $M_v > 12$ , although there are some reasons to be cautious. The difference at faint magnitudes between the results based on the D’Antona & Mazzitelli and Siess et al. isochrones illustrates that there is some model dependency. The Siess et al. isochrone is fainter than the D’Antona & Mazzitelli isochrone in the  $V$  vs  $V - I_c$  CMD at  $V - I_c \simeq 3$ , and as a result an extra 15 faint stars are identified as candidate members. However, it is unrealistic to suppose that the steep decline seen even for the Siess et al. luminosity function at  $M_v > 12$  could be reversed by a model isochrone that is even fainter at red colours. For one thing, one would start to lose candidate members from above the original isochrones and for another, there would be a distinct possibility of heavy contamination of the selected candidates by field stars, thus increasing the actual decline in the luminosity function.

The second feature of the luminosity functions worth commenting on is the presence of a strong “Wielen dip” at  $7 < M_v < 8$  (Wielen 1974; Upgren & Armandroff 1981; Bahcall 1986). This feature has been seen in several other open clusters and the field (see Jeffries et al. 2001), but is the first time it has been seen in such a very young cluster. In NGC 2547 the appearance of the dip is enhanced



by the likelihood of contaminating field objects between  $5.75 < M_v < 7.0$ , but it is most certainly real as can be judged from the scarcity of objects seen in the  $V$  vs  $V - I_c$  CMD between  $1.4 < V - I_c < 1.7$ . The dip is most likely caused by a change in slope of the mass-luminosity relation, rather than a discontinuity in the mass function (see below).

In Fig.18b we compare the completeness-corrected luminosity function of NGC 2547 (derived from the D’Antona & Mazzitelli isochrones) with a normalized field star luminosity function (obtained from Reid & Hawley 2000). In a young cluster like NGC 2547 we would expect there to be relatively more short-lived, bright, high mass stars, so we normalise the field luminosity function to NGC 2547 at  $8 < M_V < 10$ . The expected excess of bright stars at  $M_V < 4$  is indeed present in NGC 2547, but there also seems to be a deficit of faint stars at  $M_v > 10$ . The deficit is only marginally reduced if the Siess et al isochrones are used instead, but may actually be worsened if there are interloping non-members in the faint NGC 2547 sample. Of course, the steep decline in the NGC 2547 luminosity function may not be the signature of a falling *mass* function. The shape of the relationship between mass and luminosity (and  $M_v$ ) will be different from that for field stars in a very young cluster like NGC 2547.

## 15 THE MASS FUNCTION

The cluster mass function (MF) is estimated by calculating the mass of each candidate member using a mass- $V$  relationship derived from the isochrones that were used to fit the cluster CMDs. We define the MF using the form  $dN/d\log M \propto M^{-\alpha}$ , where the canonical initial mass function (IMF) for field stars derived by Salpeter (1955) would have  $\alpha = +1.35$ . Unresolved binarity is a problem for this technique in two ways: A binary star that appears above the single star cluster locus will be treated as one star with a slightly higher mass than either of its two components. The second problem is that binary stars with unequal mass components ( $q < 0.5 - 0.6$ ) will have a derived primary star mass that is approximately correct, but the hidden, lower mass secondary component will not be included in the mass function. Sagar & Richtler (1991) and Kroupa (2001) show that the combination of these two effects could result in serious systematic underestimates of  $\alpha$  by between 0.3 and 1, depending on the mass range considered, the binary fraction and the steepness of the mass function.

We take a simple approach which addresses the first of these difficulties. We add 0.5 mag to the  $V$  of an object identified as a  $q \geq 0.5$  binary ( $q \geq 0.6$  for  $V < 14$ ) in the candidate member selection procedure and then put two stars with a mass appropriate for this new magnitude into the corresponding mass function bin. The second problem is less easy to deal with because we do not know what the binary fraction or distribution of mass ratios are as a function of mass. We estimate the possible effects by simulating a binary fraction and mass ratio distribution among those stars considered single (see below). Attempting to correct the observed mass function for binarity is important if one wants to calculate a total mass or estimate the true mass function. It is not an issue when comparing one cluster with another or with the field, so long as corrections have been applied in

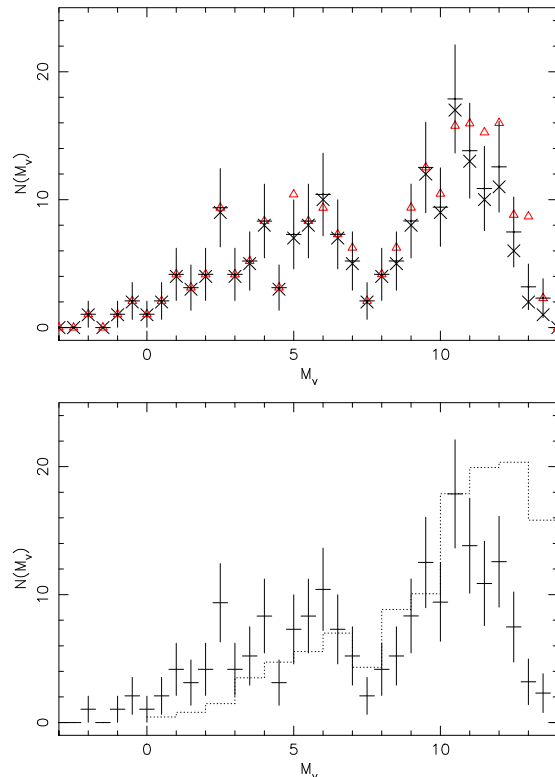


**Figure 18.** Top: The derived luminosity functions. The functions derived using members selected with the D’Antona & Mazzitelli (1997) isochrones are shown both with and without completeness correction (error bars and diagonal crosses respectively). The completeness-corrected function using the Siess (2000) selected members are marked by triangles. Bottom: The corrected NGC 2547 luminosity function (derived using the D’Antona & Mazzitelli isochrones) vs that for the field. The luminosity functions have been normalized for  $8 < M_V < 10$ .

the same way (or not at all) and there are no significant differences in binary fraction or mass ratio distribution. There is only marginal evidence for an enhanced binary fraction in younger clusters compared to the field (Bouvier et al. 2001), but we know little about the evolution of mass ratio distributions. In field stars and the Pleiades,  $q$  has a relatively flat distribution between 0.1 and 1, although there is some evidence for a small rise in frequency at  $q \simeq 0.3$  (Duquennoy & Mayor 1991; Kähler 1999). In this paper we will quote and display as our main results the mass functions after applying our correction for binaries with large  $q$ . We choose to do this because it is a simple scheme that could easily be applied to any observational dataset. We will however examine the effects of not including this correction or attempting to include a simulated binary population with small  $q$ .

We show the mass- $V$  relations used in Fig. 19. The mass- $V$  relationships from the isochrones are only well calibrated to  $3M_{\odot}$ . This is the maximum mass in the D’Antona & Mazzitelli models, but it is also approximately the point at which  $B - V$  becomes bluer than the available Pleiades objects used to calibrate the colour- $T_{\text{eff}}$  relation. For the four stars with higher masses we have used a mass- $V$  relationship

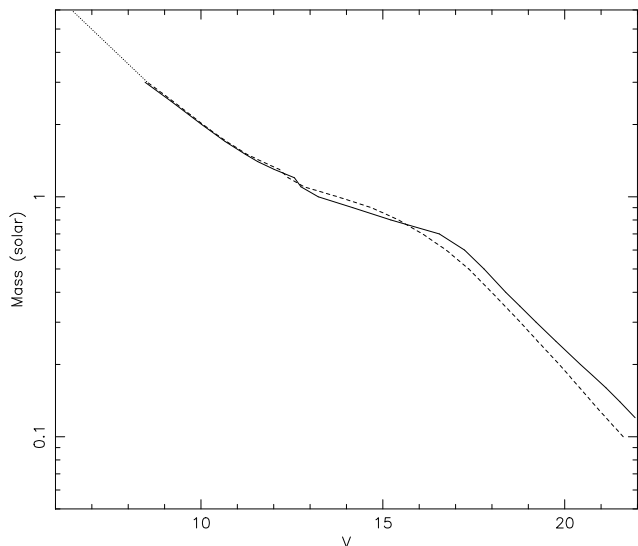


**Figure 19.** The adopted mass vs  $V$ -magnitude relationships. The dashed line is from Siess (2000), the solid line from D’Antona & Mazzitelli (1997), and the dotted line from Schaller (1992).

from the models of Schaller et al. (1992), which is shown as a dotted line in Fig. 19.

The derived MFs are shown in Fig. 20. MFs that are both corrected and uncorrected for completeness are shown for the D’Antona & Mazzitelli isochrones, so that the reader can judge what effect these corrections have. The corrections have an almost negligible effect on the MF shape until the very lowest masses. The effects of field star contamination in our sample will be seen as an overestimate of the MF. For  $14.0 < V < 15.25$ , where we expect the contamination could be as high as 40 percent, this corresponds to a mass range of  $0.8 < M < 1.0M_{\odot}$ . This contamination is therefore confined to the one high point in the MF at  $\log(M/M_{\odot}) = -0.05 \pm 0.05$ , which we ignore when fitting the mass function (see below).

At slightly fainter magnitudes and lower masses, we see that the shallower gradient in the D’Antona & Mazzitelli mass- $V$  relation at  $V \sim 16$  has almost completely removed the “Wielen dip” that was seen in the luminosity function. The same cannot be said for the Siess et al. mass- $V$  relation and derived MF, where there still appears to be a significant depression for  $-0.3 < \log(M/M_{\odot}) < -0.1$ .

If we were to consider the evidence from the D’Antona & Mazzitelli results alone, we might have concluded that there were indications that the MF turns downward at  $M < 0.2M_{\odot}$ . Comparison with the results from the Siess et al. models show that such a conclusion would be premature. There are two basic reasons for the discrepant behaviour at low masses. First, the Siess et al. isochrones follow a somewhat lower path (by  $\sim 0.1$  mag) in the  $V$  vs  $V - I_c$  CMD and as a result there are an extra 15 stars included in the luminosity function at faint magnitudes (see Fig.18). Second, the mass- $V$  relationship for the two sets of models are similar above  $1M_{\odot}$ , but become significantly different at low masses. The Siess et al. models yield a lower mass for the same  $V$  magnitude, which has the effect of moving stars into lower mass bins when compared with the D’Antona & Mazzitelli MF.

There are additional reasons to be cautious in inter-

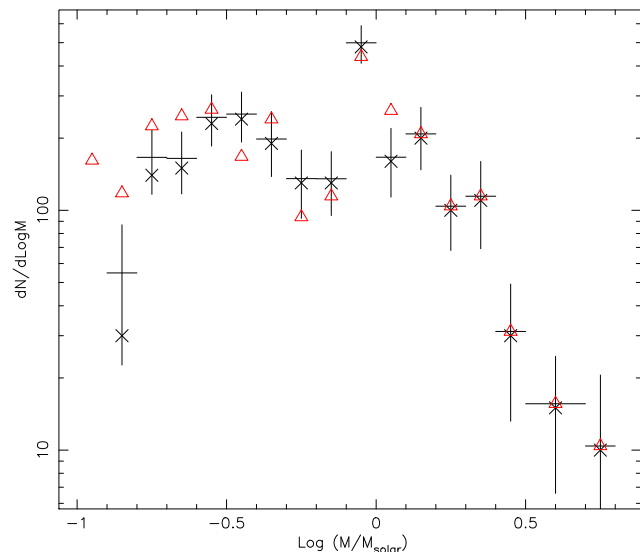


**Figure 20.** The derived mass functions. The triangles use the models of Siess (2000) the crosses those of D’Antona & Mazzitelli (1997); neither are corrected for completeness. The error bars are the points derived from D’Antona & Mazzitelli (1997), corrected for completeness.

preting the low-mass MF, not connected with the chosen evolutionary models. Our photometric calibration at  $V - I_c$  is not tightly constrained for very red stars. Only three standards were measured with  $V - I_c > 2$  (the reddest of which had  $V - I_c = 2.7$ ), and although these stars are well fitted with a colour term very close to unity (i.e. the filter combination almost perfectly matches the Cousins system), we have to realize that the colours and magnitudes for redder stars are based on an extrapolated calibration. This colour limit corresponds to approximately  $V \simeq 18.5$  in the cluster, or masses of about  $0.35M_{\odot}$ . A change in the colour calibration beyond this point could result in a different number of stars being selected as members of the cluster (because the isochrone shape would change). It would also have the more minor effect of changing the deduced masses for the cluster candidates, if their  $V$  magnitudes were significantly altered. However, the appearance of the CMD gives us some confidence that this is not likely to yield MFs outside of the range encompassed by the two sets of evolutionary models that we have used here.

The MFs we have derived show the same general features that have been seen in the field and in other young cluster like the Pleiades, with a steep increase from high to low masses which flattens below  $1M_{\odot}$ . We have parameterized the MFs by fitting power laws of the form  $dN/d \log M \propto M^{-\alpha}$  to the sections from  $0.1 < M < 0.8M_{\odot}$  (stopping at  $0.16M_{\odot}$  for the D’Antona & Mazzitelli derived MFs) and  $1 < M < 6M_{\odot}$ . We find  $\alpha = 0.20 \pm 0.25$  or  $0.20 \pm 0.18$  for the low-mass stars using the D’Antona & Mazzitelli or Siess et al. models respectively, and  $\alpha = 1.8 \pm 0.4$  or  $2.0 \pm 0.4$  for the high-mass stars.

The results for the higher mass stars seem a little steeper than the  $\alpha = 1.40 \pm 0.13$  found for intermediate mass stars in many open clusters by Phelps & Janes (1993) and also than the canonical field MF value of  $\alpha = 1.35$  found by Salpeter (1955). Some of the difference can be attributed to our technique of splitting the  $q > 0.6$  unresolved

binary systems into two stars of slightly lower masses. This practice was not adopted by the cited papers, which used a single mass- $V$  relation irrespective of binary status. This would not greatly affect the results if binary fraction were independent of mass *and* there were no high-mass cut-off to the distribution. However this is not the case in our data, which is limited to  $M < 6M_{\odot}$ . We therefore find that if we were to adopt the same procedure as the previous work, our MFs would be less steep and  $\alpha$  reduced to  $1.3 \pm 0.4$ .

The results for low-mass stars are very similar to those derived for the Pleiades (where  $\alpha \simeq 0$  for  $0.3 < M < 1.0M_{\odot}$  – Meusinger et al. 1996), M35 (where  $\alpha = -0.2$  for  $0.2 < M < 0.8M_{\odot}$  – Barrado y Navascués et al. 2001) and the field (where  $-0.1 < \alpha < +0.3$  for  $0.1 < M < 0.6M_{\odot}$  – Gould et al. 1997; Kroupa 2001). We find that our treatment of  $q > 0.5$  binary systems has a small effect. If we had not used this correction, our  $\alpha$  would be smaller by 0.2 and thus approximately zero.

The total mass of the cluster (inside the deep survey area) can now be estimated by summing the masses of the individual stellar systems. A simple integration of the mass function yields  $190M_{\odot}$  down to stellar masses of  $0.1M_{\odot}$  (irrespective of which evolutionary model is chosen). This figure contains a partial correction for those binary systems with  $q > 0.5$ , which accounts for  $30 \pm 4$  percent of the total number of stellar systems. This binary fraction is a little higher than for equivalent systems in G-type field stars (22 percent – Duquennoy & Mayor 1991), but very similar to the 26 percent found by similar techniques among the G and K stars of the Pleiades and NGC 2516 (Stauffer et al. 1984; Jeffries et al. 2001). There is some evidence that the binary fraction among lower mass field stars is smaller (30-40 percent), but that they are more inclined to be found in high mass ratio systems (Fisher & Marcy 1992). If we were to assume a flat  $q$  distribution down to  $q = 0$ , then our measurements are consistent with a total binary fraction of about 60 percent for NGC 2547. Adopting the Duquennoy & Mayor (1991) field star  $q$  distribution, we would estimate a total binary fraction of about 90 percent.

To account for these hidden binary companions in  $q < 0.5$  systems, or at least illustrate what effects they might have on the mass function and total cluster mass, we simulate the unobserved binary population assuming a total binary fraction and mass ratio distribution. We assume a total binary fraction of 90 percent and then randomly randomly allocate lower mass binary companions to the “single” stars, with  $q$  drawn from the distribution proposed by (Duquennoy & Mayor 1991). We generate a mass function in the same way as previously and integrate this function to get the total mass (above  $0.1M_{\odot}$ ). The mass function is only slightly changed from those discussed above.  $\alpha$  is increased by about 0.1 for the low mass stars and unchanged for the high mass stars. The total mass of the cluster increases to about  $240M_{\odot}$ .

To compare the mass of NGC 2547 with other clusters we need also to make a correction for the fact that our deep survey area only covers a fraction of the cluster. To estimate this fraction we simply note that Clariá’s (1982) photometry of bright stars in the region appears to be complete to  $V = 12$  and covered a much larger area (50 arcmin radius) than our own. We find that 65 percent of Clariá’s proposed cluster members with  $V < 12$  (which almost entirely agree with

our own classifications where there is overlap) lie within the bounds of our deep survey area. Assuming that this fraction is mass-independent, i.e. that there is no mass segregation in this young cluster, we obtain a final estimate of the cluster mass of  $370M_{\odot}$ . This is considerably less (by factors of 3-5) than rich open clusters like the Pleiades, M35 and NGC 2516 (e.g. Meusinger et al. 1996; Barrado y Navascués et al. 2001; Jeffries et al. 2001). Thus an important result is that the mass function of NGC 2547 is very similar to that of clusters with much larger masses, providing some support for the idea that the initial mass function is universal and independent of environment (Kroupa 2002).

## 16 CONCLUSIONS

In this paper we have developed a set of algorithms for effectively dealing with the analysis of large CCD, multi-colour mosaics, with the ultimate aim of producing colour-magnitude diagrams with well-understood completeness properties. We have shown that the uncertainty estimate from these techniques is robust, and that the resulting colour-magnitude diagrams reach approximately 0.45 magnitudes deeper than the same dataset reduced using aperture photometry. We have also shown that the completeness correction technique is reliable.

To obtain the best from the software (or indeed any similar data reduction procedure), we recommend the following observing strategy.

- 1) The area to be surveyed should be divided into fields, with an overlap between each field. The reasons for this are given in Section 9, but in summary are as follows.
  - (i) Minimizing the difference between the measurements of the same stars in different fields improves the self-consistency of the catalogue.
  - (ii) The remaining differences give an estimate of the systematic calibration errors.
- 2) If magnitudes or positions of bright stars are required (for example as fiducial stars for follow-up fibre spectroscopy), a single short exposure should be made for each field in each band.
- 3) The signal-to-noise ratio for the faintest stars should then be built up through at least three longer exposures. There are two reasons for preferring this to a single, longer exposure.
  - (i)  $\chi^2$  can be used to distinguish spurious events in a single frame from objects which appear in all frames (Section 7).
  - (ii) The final effective profile correction is a mean of several measurements, yielding greater precision.

We have applied our techniques to the young open cluster, NGC 2547. From X-ray selected members of the cluster in the  $B - V, V$  and  $V - I_c, V$  colour-magnitude diagrams we have estimated a new (model-dependent) intrinsic distance modulus of 8.00-8.15 and an age of 20-35 Myr. The fitted isochrones have been used to photometrically select cluster members and derive completeness-corrected luminosity and mass functions between  $0.1$  and  $6M_{\odot}$ . The luminosity function shows some evidence for a lack of stars

with  $M_v > 10$  when compared with the field and Pleiades functions. There is also strong evidence for a “Wielen dip” at  $M_v \sim 8$ . We find that this luminosity function structure is largely absent in the mass function, which shows great similarity to the mass functions found in the field and other open clusters. The total cluster mass (down to stars of  $0.1M_\odot$ ) is about  $190M_\odot$ , or  $370M_\odot$  if we make approximate corrections for unresolved binaries and stars lying outside our survey area. Thus NGC 2547 is a factor of 3-5 less massive than some older open clusters like the Pleiades, M35 and NGC 2516, yet has an extremely similar mass function.

## ACKNOWLEDGMENTS

We are grateful to PPARC for supporting TN through the advanced fellowship programme, SAT through the studentship programme and for research grant support for EJT. CRD was supported by a Nuffield Undergraduate Bursary (NUF-URB00). We would like to thank the director and staff of the Cerro Tololo Interamerican Observatory, operated by the Association of Universities for Research in Astronomy, Inc., under contract to the US National Science Foundation. Computing was performed at the Keele and Exeter nodes of the Starlink network, funded by PPARC.

## REFERENCES

- Alcock C., et al 1996, *ApJ*, 461, 84  
 Arnouts S., Vandame B., Benoist C., Groenewegen M. A. T., da Costa L., Schirmer M., Mignani R. P., Slijkhuis R., Hatziminaoglou E., Hook R., Madejsky R., Rit e C., Wicenc A., 2001, *A&A*, 379, 740  
 Bahcall J. N., 1986, *ARA&A*, 24, 577  
 Barrado y Navascu es D., Stauffer J. R., Bouvier J., Mart in E. L., 2001, *ApJ*, 546, 1006  
 Bertin E., Arnouts S., 1996, *A&AS*, 117, 393  
 Bessell M. S., Castelli F., Plez B., 1998, *A&A*, 333, 231  
 Bouvier J., Duch ene G., Mermilliod J. C., Simon T., 2001, *A&A*, 375, 989  
 Bouvier J., Rigaut F., Nadeau D., 1997, *A&A*, 323, 139  
 Caldwell J., Keane M., Schechter P., 1991, *AJ*, 101  
 Clari a J., 1982, *A&ASS*, 47, 323  
 D’Antona F., Mazzitelli I., 1997, *Mem. Soc. Astr. It.*, 68, 807  
 Duquennoy A., Mayor M., 1991, *A&A*, 248, 485  
 Eaton N., Draper P., Allan A., 1999, PHOTOM – A Photometry Package version 1.8-3 Starlink User Note 45.9, Starlink Project  
 Epchtein N., et al 1997, *The Messenger*, 87, 27  
 Fischer P., Kochanski G. P., 1994, *AJ*, 107, 802  
 Fisher D. A., Marcy G. W., 1992, *ApJ*, 396, 178  
 Flower P. J., 1996, *ApJ*, 469, 355  
 Gould A., Bahcall J. N., Flynn C., 1997, *ApJ*, 482, 913  
 Hambly N. C., Davenhall A. C., Irwin M. J., MacGillivray H. T., 2001, *MNRAS*, 326, 1315  
 Hambly N. C., MacGillivray H. T., Read M. A., Tritton S. B., Thomson E. B., Kelly B. D., Morgan D. H., Smith R. E., Driver S. P., Williamson J., Parker Q. A., Hawkins M. R. S., Williams P. M., Lawrence A., 2001, *MNRAS*, 326, 1279  
 Irwin M., 1997, in Rodr guez J., Espinosa A., Herrero A., S nchez F., eds, *Instrumentation for Large Telescopes (VII Canary Islands Winter School)* Cambridge University Press  
 Jeffries R., Thurston M., Hambly N., 2001, *A&A*, 375, 863  
 Jeffries R., Tolley A., 1998, *MNRAS*, 300, 331  
 Jeffries R., Totten E., James D., 2000, *MNRAS*, 316, 950  
 K hler H., 1999, *A&A*, 346, 67  
 Kalirai J., Richer H., Fahlman G., Cuillandre J.-C., Ventura P., D’Antona F., Bertin E., Marconi G., Durrell P., 2001, *AJ*, 122, 266  
 King I., 1983, *PASP*, 95, 163  
 Kroupa P., 2001, *MNRAS*, 322, 231  
 Kroupa P., 2002, *Science*, 295, 82  
 Leggett S. K., Allard F., Berriman G., Dahn C. C., Hauschildt P. H., 1996, *ApJS*, 104, 117  
 Mermilliod J. C., Rosvick J. M., Duquennoy A., Mayor M., 1992, *A&A*, 265, 513  
 Meusinger H., Schilbach E., Souchay J., 1996, *A&A*, 312, 833  
 Momany Y., Vandame B., Zaggia S., Mignani R. P., da Costa L., Arnouts S., Groenewegen M. A. T., Hatziminaoglou E., Madejsky R., Rit e C., Schirmer M., Slijkhuis R., 2001, *A&A*, 379, 436  
 Monet D., 1998, *BAAS*, 30, 1427  
 Mutchier M., Fruchter A., 1997, in *The 1997 HST Calibration Workshop with a new generation of instruments* /edited by Stefano Casertano, Robert Jedrzejewski, Charles D. Keyes, and Mark Stevens. Baltimore, MD : Space Telescope Science Institute (1997) QB 500.268 C35 1997, p. 355. Drizzling Dithered WFPC2 Images-A Demonstration. p. 355  
 Naylor T., 1998, *MNRAS*, 296, 339  
 Naylor T., Jeffries R. D., Pozzo M., 2001, in Montmerle T., Andre P., eds, *ASP Conf. Ser. 243: From Darkness to Light* p. 705  
 Phelps R. L., Janes K. A., 1993, *AJ*, 106, 1870  
 Pozzo M., Jeffries R. D., Naylor T., Totten E. J., Harmer S., Kenyon M., 2000, *MNRAS*, 313, L23  
 Reid I. N., Hawley S. L., 2000, in *New light on dark stars* Springer-Praxis  
 Robichon N., Arenou F., Mermilliod J.-C., Turon C., 1999, *A&A*, 345, 471  
 Sagar R., Richtler T., 1991, *A&A*, 250, 324  
 Salpeter E. E., 1955, *ApJ*, 121, 161  
 Schaller G., Schaerer D., Meynet G., Maeder A., 1992, *A&AS*, 96, 269  
 Siess L., Dufour E., Forestini M., 2000, *A&A*, 358, 593  
 Stauffer J. R., Hartmann L., Soderblom D. R., Burnham N., 1984, *ApJ*, 280, 202  
 Stauffer J. R., Schultz G., Kirkpatrick J. D., 1998, *ApJ*, 499, L199  
 Stetson P., 1987, *PASP*, 99  
 Stetson P., 1991, in Janes K., ed., *ASP Conf. Ser. 13: The Formation and Evolution of Star Clusters* pp 88–111  
 Stover R., Allen S., 1987, *PASP*, 99, 877  
 Totten E. J., Jeffries R. D., Hambly N. C., 2000, in Pallavicini R., Micela G., Sciortino S., eds, *ASP Conf. Ser. 198: Stellar clusters and associations: Rotation, activity and dynamos* p. 55

- Udalski A., Kubiak M., Szymanski M., 1997, *Acta Astronomica*, 47, 319
- Uppgren A. R., Armandroff T. E., 1981, *AJ*, 86, 1898
- von Hippel T., Sarajedini A., 1998, *ApJ*, 116
- Wallace P., 1998, *ASTROM – Basic astrometry program v3.6 – User’s Guide*, Starlink User Note 5.17, Starlink Project
- Wallace P., 1999, *SLALIB – Positional Astronomy Library 2.4-0 Programmer’s Manual*, Starlink User Note 67.45, Starlink Project
- Wielen R., 1974, in Contopoulos G., ed., *Highlights of Astronomy*, Vol. 3 Dordrecht: Reidel, p. 395
- York D. G., et al 2000, *AJ*, 120, 1579
- Zacharias N., Urban S., Zacharias M., Hall D., G.L. W., T.J. R., Germain M., Holdenried E., Pohlman J., F.S. G., D.G. M., Winter L., 2000, *AJ*, 120, 2131

Clariá ID	Field	Star	J2000 Position		Pixel Position		Mag.	V Error	Flag	Mag.	B-V		Flag	Mag.	V-I		Flag
			R.A.	Dec.	X	Y					Error	Error			Error	Error	
2	13	3	08 10 20.53	-49 14 13.05	936.482	1186.031	10.878	0.022	44	-1.139	0.027	44	2.270	0.030	44		
4	4	9	08 10 16.08	-49 02 5.58	44.039	220.261	10.671	0.005	44	0.401	0.007	44	0.837	0.008	44		
5	1	14	08 10 59.55	-49 17 2.86	550.354	861.607	11.107	0.005	44	0.473	0.007	44	0.975	0.008	44		
6	13	12	08 10 27.20	-49 09 51.51	774.996	533.727	10.926	0.022	44	-1.102	0.027	44	2.099	0.030	44		
7	2	10	08 09 59.20	-49 16 12.62	464.725	729.392	10.864	0.005	44	0.403	0.007	44	1.041	0.008	44		
8	7	10	08 08 41.61	-49 29 49.76	1775.237	1948.361	9.416	0.022	44	0.184	0.027	44	0.752	0.030	44		
9	2	11	08 10 7.84	-49 16 36.84	254.033	789.545	10.817	0.005	44	0.403	0.007	44	1.039	0.008	44		
12	14	10	08 09 23.65	-49 10 46.30	752.246	666.993	9.688	0.022	44	-0.039	0.027	44	0.681	0.030	44		
13	13	15	08 09 56.01	-49 19 30.08	1532.496	1978.130	10.889	0.022	44	-1.254	0.027	44	2.359	0.030	44		
14	14	3	08 09 36.66	-49 11 35.75	434.076	789.798	13.221	0.022	44	-0.635	0.027	44	-0.477	0.031	44		
15	4	13	08 09 57.52	-49 08 20.64	497.708	1155.391	10.922	0.005	44	0.387	0.007	44	0.844	0.008	44		
16	14	11	08 09 25.99	-49 11 55.83	694.830	840.222	9.812	0.022	44	-0.148	0.027	44	0.463	0.030	44		
18	18	13	08 10 20.82	-49 03 37.47	940.175	1165.762	9.836	0.022	44	0.056	0.027	44	0.264	0.030	44		
19	14	12	08 09 51.27	-49 11 15.83	77.055	739.852	120.528	101.958	88	-0.321	130.247	88	0.776	144.121	88		
21	14	13	08 08 49.85	-49 13 43.98	1577.135	1112.282	9.770	0.022	44	-0.043	0.027	44	0.416	0.030	44		
22	13	20	08 10 31.42	-49 06 31.07	672.533	33.895	10.951	0.022	44	-0.935	0.027	44	1.487	0.030	40		
23	17	13	08 09 49.49	-49 01 49.55	131.648	895.277	120.693	101.958	88	-0.312	130.247	88	0.945	144.121	88		
24	7	12	08 09 28.12	-49 25 57.69	646.604	1366.610	10.011	0.022	04	0.650	0.027	04	1.060	0.030	44		
25	7	11	08 09 49.11	-49 25 4.62	136.097	1233.820	120.563	101.958	88	-0.058	130.247	88	0.782	144.121	88		
26	14	14	08 09 52.16	-49 11 2.61	55.325	706.881	120.510	101.958	88	-0.322	130.247	88	0.771	144.121	88		
27	14	15	08 08 53.12	-49 13 49.58	1497.047	1125.950	9.940	0.022	44	-0.064	0.027	44	0.282	0.030	40		
28	18	16	08 10 42.32	-48 57 25.73	414.249	238.239	9.859	0.022	44	0.070	0.027	44	0.113	0.030	40		
30	4	18	08 10 8.41	-49 00 43.71	232.312	16.317	10.747	0.005	44	0.365	0.007	44	0.710	0.008	44		
31	2	14	08 10 6.04	-49 14 18.47	298.178	444.686	10.938	0.005	44	0.369	0.007	44	0.774	0.008	44		
32	12	13	08 11 25.84	-49 12 29.22	909.568	924.451	9.994	0.022	44	0.087	0.027	44	0.185	0.030	40		
33	19	11	08 11 8.62	-49 00 16.90	1345.094	666.306	10.209	0.022	44	0.142	0.027	44	-0.018	0.030	44		
35	7	13	08 09 30.49	-49 21 56.22	589.893	764.561	10.257	0.022	44	0.026	0.027	44	0.282	0.030	40		
36	8	13	08 10 35.94	-49 18 21.46	569.289	228.736	10.021	0.022	40	0.257	0.027	40	0.329	0.030	00		
38	12	14	08 10 48.73	-49 06 51.81	1819.852	86.366	10.103	0.016	00	0.376	0.019	00	0.489	0.021	00		
39	17	14	08 09 29.56	-49 06 16.79	619.150	1561.870	8.084	0.022	88	1.942	0.027	88	0.191	0.030	88		
41	2	17	08 09 50.64	-49 12 49.88	674.479	224.332	11.002	0.005	44	0.376	0.007	44	0.730	0.008	44		
42	18	19	08 10 38.97	-49 01 48.83	495.654	894.172	10.338	0.022	44	-0.100	0.027	44	-0.042	0.030	40		
43	2	16	08 10 13.50	-49 19 13.23	115.607	1179.280	11.015	0.005	44	0.405	0.007	44	0.927	0.008	44		
45	7	14	08 09 38.12	-49 18 40.96	404.576	277.555	10.802	0.013	00	0.259	0.016	00	0.307	0.017	00		
48	18	21	08 10 26.68	-49 06 53.48	795.559	1654.082	10.521	0.022	00	0.213	0.027	00	0.287	0.030	00		
49	2	19	08 09 50.58	-49 13 19.90	675.937	299.162	11.128	0.005	44	0.362	0.007	44	0.668	0.008	44		
50	7	15	08 08 45.74	-49 23 47.67	1678.509	1045.302	10.728	0.022	00	0.292	0.027	00	0.328	0.030	00		
51	14	17	08 09 46.11	-49 14 27.08	202.980	1216.712	10.680	0.022	00	0.248	0.027	00	0.344	0.030	00		
52	18	22	08 09 51.93	-49 00 25.36	1649.861	689.060	10.715	0.022	00	0.143	0.027	00	0.160	0.030	00		
53	13	28	08 10 31.52	-49 16 43.80	667.636	1561.296	11.332	0.022	04	0.526	0.027	04	5.883	0.030	48		
54	9	12	08 10 46.62	-49 17 31.53	1875.384	108.580	10.760	0.013	00	0.442	0.016	00	0.540	0.017	00		
56	7	16	08 09 35.57	-49 27 1.55	465.125	1525.564	10.777	0.022	00	0.440	0.027	00	0.558	0.021	00		
57	9	13	08 11 37.83	-49 29 36.49	623.488	1911.992	6.388	0.022	88	2.308	0.027	88	1.045	0.030	88		
58	19	13	08 11 3.25	-49 00 37.78	1476.825	718.776	10.881	0.022	00	0.283	0.027	00	0.356	0.030	00		
60	13	3728	08 09 48.31	-49 09 38.19	1725.986	503.403	18.503	0.030	11	1.025	0.143	11	0.610	0.079	11		
61	8	17	08 10 24.41	-49 23 17.45	848.941	967.079	10.889	0.022	00	0.198	0.027	00	0.300	0.030	00		
62	14	20	08 09 26.69	-49 14 37.30	676.996	1242.751	10.887	0.022	00	0.306	0.027	00	0.367	0.030	00		
63	13	33	08 10 27.71	-49 12 10.01	761.754	878.948	11.353	0.022	04	0.226	0.024	04	0.863	0.026	40		
64	2	23	08 10 16.70	-49 15 17.62	37.895	591.971	11.155	0.005	44	0.320	0.007	44	0.554	0.008	44		
65	7	17	08 09 30.51	-49 20 44.74	589.619	586.347	11.081	0.022	00	0.356	0.027	00	0.427	0.030	00		
66	8	19	08 10 13.53	-49 20 44.05	1114.921	585.299	10.970	0.022	00	0.478	0.027	00	0.606	0.030	00		
67	19	14	08 11 11.36	-49 04 44.47	1276.119	1332.991	11.051	0.022	00	0.327	0.027	00	0.447	0.030	00		

Clariá ID	Field	Star	J2000 Position		Pixel Position		V			B-V			V-I		
			R.A.	Dec.	X	Y	Mag.	Error	Flag	Mag.	Error	Flag	Mag.	Error	Flag
68	18	23	08 10 0.89	-49 08 32.58	1426.108	1902.766	10.983	0.022	00	0.452	0.027	00	0.580	0.030	00
69	13	38	08 10 27.14	-49 10 29.45	776.268	628.323	11.450	0.022	04	0.878	0.024	04	1.361	0.026	40
70	12	16	08 11 22.34	-49 09 14.84	996.397	440.142	11.137	0.022	00	1.355	0.027	00	1.424	0.030	00
71	14	22	08 08 50.38	-49 16 16.43	1562.658	1492.286	11.382	0.022	00	0.422	0.027	00	0.557	0.030	00
72	17	17	08 09 14.03	-49 04 3.30	1000.210	1229.880	11.412	0.022	00	0.366	0.027	00	0.420	0.030	00
73	8	21	08 09 47.31	-49 19 42.72	1754.214	434.597	11.435	0.022	00	1.322	0.024	00	1.374	0.030	00
74	14	21	08 09 2.85	-49 16 9.65	1258.535	1474.364	11.460	0.022	00	0.211	0.027	00	0.219	0.031	00
75	9	15	08 10 40.05	-49 17 47.30	2035.372	148.636	11.565	0.016	00	1.187	0.018	00	1.202	0.021	00
76	8	22	08 10 11.66	-49 22 27.71	1159.697	843.840	11.601	0.022	00	0.556	0.027	00	0.635	0.030	00
77	8	24	08 10 16.64	-49 21 32.72	1038.872	706.433	11.625	0.022	00	1.772	0.024	00	1.929	0.030	04
78	3	25	08 11 5.62	-49 03 19.43	405.379	381.260	11.705	0.005	00	0.977	0.006	00	1.087	0.030	00
79	3	24	08 10 39.83	-49 04 38.04	1036.966	578.271	11.604	0.022	00	0.465	0.027	00	0.614	0.008	00
80	18	29	08 10 18.37	-49 06 46.32	999.032	1636.669	11.870	0.005	00	0.536	0.006	00	0.664	0.006	00
81	3	26	08 10 35.30	-49 06 28.31	1147.143	853.403	11.808	0.022	00	0.242	0.027	00	0.292	0.006	00
83	3	27	08 10 49.85	-49 11 25.84	789.433	1594.123	11.799	0.005	00	0.466	0.006	00	0.593	0.006	00
84	18	27	08 10 1.44	-48 58 25.49	1417.666	389.411	11.881	0.022	00	0.212	0.027	00	0.272	0.031	00
85	8	28	08 10 25.25	-49 18 58.77	829.951	322.177	12.031	0.022	00	0.563	0.028	00	0.709	0.031	00
86	3	29	08 11 17.43	-49 06 15.21	115.758	819.153	12.021	0.003	00	0.976	0.004	00	1.098	0.005	00
87	1	32	08 11 20.74	-49 13 10.18	33.468	281.191	12.016	0.002	00	0.536	0.003	00	0.650	0.003	00
88	12	24	08 11 28.86	-49 10 52.64	836.330	683.557	12.103	0.022	00	0.445	0.028	00	0.515	0.026	00
89	18	30	08 10 34.32	-49 00 49.89	610.018	747.421	11.985	0.022	00	0.444	0.027	00	0.567	0.031	00
90	3	35	08 10 29.53	-49 09 0.68	1287.120	1233.552	12.173	0.005	00	1.400	0.006	00	1.434	0.008	04
91	3	36	08 10 20.14	-49 09 38.66	1516.448	1328.978	12.157	0.004	00	1.342	0.005	00	1.312	0.007	00
92	18	32	08 10 23.04	-49 00 30.32	886.729	699.135	12.098	0.022	00	0.203	0.027	00	0.318	0.026	00
93	3	37	08 11 11.59	-49 05 21.17	258.985	684.537	12.190	0.004	00	1.747	0.005	00	1.937	0.030	00
94	18	35	08 10 45.45	-49 01 7.05	336.790	789.856	12.108	0.005	00	0.497	0.006	00	0.662	0.006	00
95	3	38	08 10 27.13	-49 11 50.45	1344.498	1656.863	12.267	0.003	00	1.078	0.004	00	1.192	0.005	00
96	1	36	08 10 57.89	-49 18 15.75	590.523	1043.333	12.257	0.004	00	1.583	0.005	00	1.706	0.018	00
97	14	32	08 09 47.32	-49 13 5.35	173.533	1012.938	12.301	0.016	00	0.536	0.017	00	0.698	0.019	00
98	1	38	08 11 0.67	-49 15 15.04	523.348	592.822	12.338	0.005	00	1.507	0.006	00	1.536	0.026	00
99	3	39	08 10 34.72	-49 08 40.21	1160.424	1182.160	12.385	0.003	00	0.561	0.004	00	0.686	0.005	00
100	8	35	08 10 9.29	-49 20 54.14	1218.054	610.737	12.449	0.015	00	0.586	0.019	00	0.771	0.022	00
101	3	48	08 10 56.58	-49 09 0.59	625.518	1231.824	12.535	0.003	00	0.386	0.004	00	0.525	0.005	00
102	2	40	08 10 12.23	-49 13 5.83	147.023	263.520	12.500	0.002	00	0.565	0.002	00	0.690	0.002	00
103	3	53	08 10 58.55	-49 08 26.04	577.501	1145.637	12.764	0.003	00	1.027	0.004	00	1.147	0.005	00
104	18	46	08 10 24.87	-49 01 49.74	841.404	897.015	12.664	0.003	00	0.605	0.004	00	0.730	0.005	00
105	2	33	08 10 1.67	-49 22 6.38	403.478	1611.086	13.086	0.003	00	1.342	0.004	00	1.361	0.005	00
106	1	52	08 10 33.81	-49 11 24.90	1180.583	20.619	12.815	0.002	00	1.116	0.003	00	1.208	0.004	00
107	1	53	08 11 5.23	-49 13 40.42	412.225	356.847	12.938	0.002	00	0.424	0.003	00	0.559	0.003	00
108	3	71	08 10 24.55	-49 08 48.84	1409.036	1204.441	13.190	0.003	00	0.544	0.004	00	0.686	0.005	00
109	1	61	08 10 48.17	-49 23 38.66	825.958	1848.613	13.173	0.003	00	0.690	0.004	00	0.782	0.005	00
110	13	93	08 10 15.42	-49 11 9.77	1062.406	729.484	13.209	0.002	00	0.756	0.003	00	0.892	0.004	00
111	3	93	08 11 0.11	-49 06 44.44	539.878	892.355	13.289	0.003	00	0.708	0.004	00	0.810	0.005	00
112	3	73	08 10 29.37	-49 08 2.56	1291.456	1088.710	13.310	0.003	00	0.380	0.004	00	0.481	0.005	00
113	13	148	08 10 27.05	-49 08 49.05	778.787	378.041	13.239	0.003	00	0.697	0.004	00	0.830	0.005	00
114	13	300	08 10 25.77	-49 08 12.73	810.332	287.572	13.536	0.003	00	0.964	0.004	00	1.167	0.005	00
115	3	94	08 10 33.24	-49 07 38.72	1196.981	1029.006	13.420	0.003	00	1.382	0.004	00	1.444	0.005	00
116	3	88	08 10 34.84	-49 08 17.60	1157.514	1125.817	13.474	0.003	00	0.481	0.004	00	0.640	0.005	00
117	1	83	08 11 3.48	-49 13 26.53	455.192	322.276	13.537	0.002	00	0.567	0.003	00	0.715	0.003	00
118	1	166	08 10 40.37	-49 21 50.95	1016.383	1580.579	13.948	0.003	00	0.627	0.004	00	0.764	0.005	00

Optimal photometry for colour-magnitude diagrams and its application

See Sections 5 and 7 for 1=non-stellar; 2=too close to detector edge; 3=fit to sky histogram failed; 4=saturated; 8 =bad pixel; 9=negative counts.

This paper has been typeset from a  $\text{\TeX}$ / $\text{\LaTeX}$  file prepared by the author.